Università degli Studi di Trento
Facoltà di Scienze Matematiche, Fisiche e Naturali
Dipartimento di Fisica

Tesi di Dottorato di Ricerca in Fisica

Fusion processes in low-energy collisions of weakly bound nuclei

Maddalena Boselli

Trento 2016

University of Trento
Faculty of Science
Department of Physics

Ph.D. Thesis

Fusion processes in low-energy collisions of weakly bound nuclei

Maddalena Boselli

Thesis Advisor:
Dr. Alexis Diaz-Torres (Department of Physics, University of Surrey, UK)

Trento 2016

Acknowledgments

Vorrei ringraziare Alexis per la grande pazienza con cui durante questi anni ha risposto a tutte le mie innumerevoli e spesso sciocche domande. Per i consigli e l'incoraggiamento che mi ha trasmesso in quei terribili momenti di ansia prima di ogni seminario o presentazione. Ma soprattutto per la comprensione con cui ha reagito ogni volta che non riuscivo a dare il massimo.

Un grazie speciale va alla mia famiglia, che per tutto questo tempo ha chiuso un occhio, e talvolta tutti e due, di fronte ai miei sbalzi di umore nei momenti di sconforto. Grazie alla mia mamma e a mio papa' per avermi dato l'opportunita' di concentrarmi e lavorare, in special modo durante le ultime settimane. Grazie a mio fratello per avermi lasciato stampare fin troppe copie della tesi e solo perche' volevo correggerla a mano. Grazie a Chiara per essermi stata vicina dall'inizio alla fine, come sempre, ne troppo, ne troppo poco.

E grazie a Daniel, per tutto il tempo, la pazienza e l'impegno e l'amore con cui mi ha sempre ascoltato e cercato di insegnare a fare le cose con stile. Per avermi sgridato quando cedevo alla pigrizia e per essermi stato vicino ed avermi fatto ridere quando ne avevo piu' bisogno.

I would like to thank Alexis for the big patience he had during these years while answering to my uncountable, and often silly, questions. For the advices and support that he transmitted to me in those terrible moments of stress just before every seminar or talk. But especially, thank you for your understanding every time I could not give the best out of me.

A special thanks goes to my family, that for all this time did not pay attention to my bad moods during hard moments. Thanks to my mom and dad for giving me the opportunity to focus and work, especially during these last weeks. Thanks to my brother who allowed me to print so many copies of the thesis just because I preferred to correct it by hand on paper. Thanks to Chiara for being close to me all the time, as usual, neither too much, nor too few.

And thanks to Daniel, for all the time, patience effort and love he put in listening to me all the time any time, and in trying to teach me how to do things properly. For yelling at me when I was lazy and for being close to me and making me laugh when I needed it the most.

Contents

Preface

The present thesis deals with the study of nuclear reactions of weakly-bound few-body nuclei with stable targets at energies around the Coulomb barrier. A weakly-bound nucleus is characterized by having low binding energy and thus large probability to undergo a breakup during the interaction with another nucleus. The effect of breakup on other reactions such as fusion is still not well understood and represents an interesting issue to study in detail. Among weakly-bound nuclei, there are some which are particularly interesting to study because of their peculiar structure and the key role they play in astrophysics: the *halo nuclei*.

Halo nuclei, such as ^{6}He, ^{11}Li and ^{19}C differ from ordinary nuclei by having a specific structure where a compact core is surrounded by a cloud, a halo, of loosely bound nucleons. The valence nucleons are relatively far away from the core – halo nuclei have their effective radius much larger compared their stable isotopes. This, together with their other properties, affects the dynamics of their interactions with other nuclei.

Understanding in detail how their peculiar properties affect the mechanism with which these exotic isotopes interact with ordinary nuclei is particularly relevant for astrophysics as there are processes, such as the formation of heavy elements or the evolution of massive stars, which strongly depend on understanding of reactions where halo nuclei are involved. The reaction dynamics of halo nuclei is believed to be different compared to their stable isotopes because of their different structure and characteristics. A deeper knowledge of their properties is necessary for better understanding of how they interact. At the same time, learning more about their reaction dynamics could provide information about their intrinsic structure. Unfortunately the properties of such exotic nuclei cannot be tested and studied directly by means of standard spectroscopic techniques due to difficulties in performing measurements. Such nuclei don't occur naturally and need to be synthesized in laboratories and, in addition to this, their life time is so short that highly efficient detector systems are required in order to observe them.

Nowadays there are many facilities around the world where beams of exotic nuclei are produced and used, mostly in inverse kinematics, to investigate the properties of halo nuclei through their reactions. An example is the ISAC facility at TRIUMF (Canada), where one of the experiments related to halo nuclei focuses on exploring the structure of

the ^{11}Li nucleus. Measuring the elastic scattering of ^{11}Li on a lead target and studying the deviations from the predictions based on the well understood Rutherford scattering, it is possible to extract information on the halo nature of ^{11}Li isotope [1]. Measurement of the breakup reaction of ^{11}Li on lead could also provide useful information [2]. In Europe, at the ISOL facility SPIRAL at GANIL (France) many experiments are planned to study properties of halo nuclei. Examples are the study of the effect of the weak binding and tunnelling of halo nuclei on their fusion dynamics through the measurement of fusion, breakup, transfer, and elastic cross sections for ^{6,8}He on ^{63,65}Cu and ^{188,190,192}Os [3] and for ^{8}He on ^{197}Au [4]. Another research facility where reactions with halo nuclei are studied is ISOLDE at CERN where, for example, the elastic scattering and reaction cross sections for ^{9,10,11}Be on a ^{64}Zn target are measured [5]. At FRIB facility (USA), study of exotic elements such as ^{60}Ca or elements ranging from ^{48}Ni to ^{80}Ni are planned (see [6] for further details). Other facilities where many experiments involving exotic nuclei are planned are FAIR (Germany) [7], at RIBF (Japan) [8].

The thesis is organized as follows: in Chapter 1 the physical motivation for the study of the reaction mechanisms of weakly-bound nuclei at low-energies is given together with a review of available theoretical models used to describe them. Chapter 2 describes in details the theoretical model used in our calculations. In chapter 3 results of our calculations are presented. In the last Chapter 4 a short summary of the main results is given and future possible improvements of the methodology are briefly discussed.

Part of the content of this thesis have been published in Phys.Rev.C 92 (2015) 044610.

Chapter 1

Introduction

Modern nuclear physics aims at understanding and interconnecting the nature from large (astrophysical systems), to small (hadrons) scales. Research covers a broad range of topics, from issues related to the synthesis of elements and the stellar evolution, to the study of the properties of nuclei [9]. A lot of effort is put to investigate the key nuclear reactions which are responsible for the creation of heavy elements, control explosive astrophysical events like supernovae and X-ray burst and govern the stellar evolution. To describe the process of nucleosynthesis in very dynamical environment such as stellar explosions is complicated because many different factors that are biased by large uncertainties have to be considered simultaneously. Often experimental measurements in the relevant energy range are missing or affected by too large errors and cannot provide the information which are needed to constrain theoretical models. From the theoretical point of view, some quantities have thus to be treated as free parameters, although they depend microscopically on nuclear structure and reaction mechanism. Moreover, performing this kind of calculations requires in general a lot of computational power and is very time consuming. A lot of theoretical work has being doing in developing more sophisticated models trying to include, among the quantities which are used as an input to the model, results coming from microscopic theories. On the experimental side, attention is given to perform more accurate measurements by developing advanced technology (detector, beam production techniques) and by planning more efficient experimental setup.

Going to nuclear physics at small scales, there is a lot of activity in studying the connection between the properties of nuclei, such as binding energies, radii, decay and energy spectra and the underlying theory QCD. Building a comprehensive description of nuclei starting from first principles, *ab initio*, represents a great challenge for theory as, the more experimental data become more and more accurate, the more is needed a theory which would be able to explain such data, provide predictions and error estimate. To achieve this, high quality nucleon–nucleon (NN) interactions and three nucleon forces (3NF) should be employed and many-body correlations and dynamics should be properly taken into account. During the last years, the existing theories have been extended and improved and more

sophisticated algorithms have been written to take advantage of the growing computing power of super computer which allows to go beyond the limits of previous calculations.

Where do halo nuclei come into the game? The exact processes which lead to the formation of heavy elements and drive explosive astrophysical events are still not completely known as they consist in a complicated interplay of different types of nuclear reactions, such as fusion, decay, proton or neutron capture, which mostly involves exotic, radioactive nuclei. These nuclei usually present an excess of number of neutrons N with respect to the number of protons Z or viceversa. Due to the large value of the ratio $\frac{N}{Z}$ (or the reciprocal) they are highly unstable and decay very fast. Halo nuclei exhibit peculiar characteristics which strongly affect the way they interact with other nuclei. A good knowledge of their properties is crucial as it would allow a better understanding of how the reactions where they are involved proceed. The problem is that their properties are still not well understood and cannot be explained by the models which describe ordinary stable nuclei.

Halo nuclei can also be used as a tool to explore the structure of the NN interaction. They behave differently from ordinary nuclei: larger radii, weak binding energies, spin-parity inversion of bound states and the vanishing of ordinary magic numbers were observed. Studying how these properties of nuclei change going from ordinary stable nuclei to the limits of the nuclear chart where exotic nuclei live and comparing theoretical predictions with data, provides a test for the quality of the model of the NN interaction.

1.1 Halo nuclei

A *halo* nucleus can be described as an object consisting of a compact core and few (one or two usually) valence nucleons which are weakly bound to the core and spatially decoupled from it. The valence nucleons should be in low relative angular momentum state (s or p wave) in order not to be confined by the centrifugal barrier. The existence of halo nuclei is due to a quantum effect. The interaction between the core and the valence nucleons is short-range and, according to classical mechanics, the valence nucleons cannot be located outside the range of the potential being still bound to the core. But the tunnelling effect allows this to happen and for this reason the valence nucleons can be found for a limited time in a volume which is beyond the range of the binding potential.

Halo nuclei have first been discovered in 1985 when Tanihata and his collaborators measured the interaction cross section of helium and lithium isotopes and extract their mass radii from it. They obtained for ^{6}He and ^{11}Li values that could not be explained

using the $A^{1/3}$ dependency which works well for stable nuclei [10]. Later on, in 1987, Hansen and Jonson suggested this phenomenon to be due to the halo feature [11]. Since then, a lot of work has been done in order to explain the properties and structure of halo nuclei and how they interact with stable nuclei.

During the '80 and '90, the first theoretical nuclear structure models of halo nuclei were developed: they were treating them as two,three-body systems composed of an inert, compact core and one or two valence nucleons. They could only provide good estimates for some key features. One of the limitations of this class of models is that, reducing the A-body wave problem to a 3-body one, the antisymmetrization of the system is not treated properly. In addition to this, due to the simplicity for a halo nucleus to dissociate, excitations to the continuum play an important role concerning the reaction mechanism and need to be taken into account. To overcome these limitations, started the era of microscopic, *ab initio* models. The advantage they brought with respect to the few-body structure models lies in the fact that the antisymmetrization is now fully treated and that realistic nucleon–nucleon potentials including 3-body forces are employed for the interactions among constituents. Some of the models which achieved very good results are the *Green Function Monte Carlo* method [12], the *No Core Shell Model* [13] and its extensions to include the continuum (No Core Shell Model/Resonating Group Method, NCSM/RGM [14] and No Core Shell Model with Continuum, NCSMC) [15], the *Coupled Cluster* method [16], the *Hyperspherical Harmonics* and the *Halo Effective Field Theory* (HEFT) [17], [18]. The biggest limitation of such models is their applicability to light-medium mass nuclei but nowadays effort is put in trying to extend their scope to heavier systems. At the same time, since from the experimental point ov vie halo nuclei are mostly studied through reactions, reaction models started to be developed as well. Some of them are the Glauber model [19], time dependent models (TD) [20], models based on the eikonal approximation [21], [22], [23] and the *Continuum Discretized Coupled Channels* (CDCC) [24]. At the present, a microscopic many-body reaction theory does not exist yet.

1.2 Halo nuclei in nuclear astrophysics

The formation of elements in the universe is controlled by several nuclear reactions but details about how the mechanism works and the location where it occurs are still not completely known. Nowadays there is an intense experimental and theoretical activity in measuring and describing accurately the reactions which are thought to be crucial in de-

termining the abundance distributions of elements. Considering the role they play in the reactions which lead to the creation of new nuclei, a detailed knowledge of the properties of halo nuclei is needed together with a sophisticated theory that is able to describe the explosive events during which heavy elements are thought to be created. Thanks to experimental observations, the possible candidates are explosive astrophysical events, such as supernova and X-ray burst [25].

The chain of such nuclear reactions is triggered by specific conditions of temperature, pressure and density of matter in the star. If the dynamics of such reactions could be better understood, it would be possible to understand the physical conditions needed for the entire mechanism to occur and this would allow to locate the site where it actually occurs.

A supernova is a powerful explosion of a massive star. Initially the star burns all its nuclear fuel until a core of Ni and Fe is created. Once no further fusion is possible (Fe is one of the most tightly bound nuclei) the core of the star becomes inert. The lack of energy release, due to the absence of further fusion reactions, breaks the equilibrium of the star, allowing an implosion driven by the gravitational force to start. While the core shrinks, temperature and pressure grow tremendously and it is under these conditions, together with a large neutron flux, that the *r-process*, is powered. It consists in a sequence of rapid neutron captures that form very neutron rich nuclei which, being highly unstable, undergo a series of fast decay until a new stable element is created. It is believed that this kind of process is responsible for the creation of elements heavier than ^{56}Fe. The NuSTAR collaboration (see [26]) will study recently-synthesized material in supernova remnants with the aim to extract information which could be useful to understand the exact stellar site where r-processes occur.

Reactions involving unstable isotopes play a key role also in the X-ray burst. In a stellar binary system, due to the gravitational attraction, matter starts to flow from the ‘donor‘ star to the ‘accretor‘ star. Material, rich in hydrogen and helium, accumulates on the surface of the accretor star and carbon is formed through hydrogen and helium burning while the temperature increases. Once large values of temperature and pressure are reached, a series of nuclear reactions starts leading to a thermonuclear runaway. The energy is released as intense short-lived X-rays that can be detected by X-ray telescope. Due to the fast reaction rates, a series of reactions occurs leading to a breakout from the hot-CNO cycle into the *rp-processes* creating heavier elements. One of the open questions is related to the mechanism which triggers the breakout from the hot-CNO cycle into the

rp-process. Measurements of the triggering reactions in the range of energies of interest require intense, low-energy radioactive beams and are planned at EURISOL, the European ISOL (Isotope-separation-on-line) facility [27].

1.3 Halo nuclei as a probe for the nucleon–nucleon interaction

An important question to which nuclear physicist are trying to answer concerns how to describe stability, structure and reactions of nuclei as a result of their interactions starting from first principles, *ab initio*. It is not possible to solve QCD in the non perturbative low energy regime which is relevant for nuclear physics, so one has to construct representations of the nucleon–nucleon (NN) interaction relying on two-body potentials. In addition to this, solving a many-body problem for bound and scattering states is a very challenging task. In particular is still not clear the role played by three and four-body forces, namely what happens to the interaction between two nucleons when the a third or fourth one are present. Indeed, accurate calculations for A=3,4 showed that two-body contributions to the NN interaction only are not enough to explain bound state properties.

For certain values (*magic numbers*) of Z and N, it has been observed that nuclei are particularly stable and this enhanced stability reveals itself in the occurrence of larger number of isotopes at the magic numbers as well as in discontinuities in nucleon binding energies. Magic numbers are interpreted in terms of the nuclear shell model and the typical level sequence of single-particle states in the excitation spectrum can be obtained using an effective NN interaction and offers a good description of the structure of nuclei near stability. On the other side, there are evidences that the standard shell model is good to describe only stable nuclei. An example of this comes from the comparison between measured and calculated elemental abundances: the peaks in the abundance pattern are connected with the magic neutron numbers of unstable neutron-rich nuclei and the calculations are not able to reproduce the experimental data. It is thus not clear how the shell structure changes for nuclei which are far from stability. For stable nuclei, closed-shell structures affect the shape of the nucleus which appears to be spherical and non rotating. But it has been discovered that nuclei with highly deformed shapes stabilized by a rotation also exist. Superdeformed nuclei have been observed and the interesting fact is that they too possess a shell structure but this is governed by a different set of magic numbers. The level structure seems to be strongly affected by the couplings between bound and contin-

uum states of nuclei for which the outer nucleons are weakly bound and occupy states close to the continuum. For such nuclei it happens that the big gap in energy levels, which is observed for a given magic number of a stable nucleus, disappears. The changes in the shell structure also affect the collective excitations that are possible within a nucleus. To find evidences of new collective modes, intense beams of radioactive neutron-rich nuclei are needed. Then, by studying the emission of gamma rays associated with the decay of the nucleus, information could be gained about the possible oscillation modes.

1.4 Theoretical description of halo nuclei

Halo nuclei are weakly bound systems for which couplings between bound and continuum states are important and the mechanism through which they react can be different from that of their stable isotopes because affected by their particular internal structure. A unified description of structure properties and reaction mechanism is therefore needed to describe reactions where they are involved. A fundamental theory which would be able to provide accurate predictions and uncertainties for a broad range of reactions is still missing because of the difficulty in dealing with many-body scattering problems and the poor knowledge of the NN interaction under the extreme conditions that occur far away from stability where halo nuclei live.

The need for an accurate knowledge of static properties of halo nuclei lead to the development over years of a variety of nuclear structure models, starting from simple few-body models, to more complicated microscopic approaches. With a two-body model that treats the halo nucleus as an inert core with a valence nucleon weakly bound to it by a short-range potential, many essential features of one-nucleon halo can be studied. For example, it is possible to obtain a realistic wave function for ^{11}Be by treating it as an inert ^{10}Be core + neutron and solving the two-body problem with a Woods-Saxon binding potential whose geometry is tuned in order to reproduce the correct neutron separation energy. This approach can be applied to any system despite of its mass, as it reduces the A-body problem to a two, three-body one, making the calculation feasible. Although the few-body dynamics and the asymptotic behaviour of the wave function are well treated, few-body models fail to reproduce many other features of halo nuclei and the reason for this is believed to be due to the fact that the antisymmetrization of the system is only treated approximately and that core excitations are completely neglected. To overcome these problems, a variety of microscopic models have been developed. There, the antisymmetrization of the system

is properly taken into account and realistic NN interactions, with the inclusion of 3NF, are employed leading to much more precise results. The biggest limitation for these *ab initio* methods lies in the fact that they can only be applied to light systems to keep the computation feasible.

At the same time, there is also a lot of activity in the field of reaction models. Due to the ease with whom halo nuclei can dissociate in the nuclear and Coulomb field of the target, couplings to the continuum need to be taken into account when developing a reaction theory. Similar to what was done for nuclear structure models, the first step consisted in building few-body reaction models. Most of the breakup theories have been developed at high fragmentation energy where several assumptions, such as the eikonal and adiabatic approximations, can be done to simplify the problem. For example, the Glauber model [19], a semiclassical model based on the eikonal approximation, provides relatively simple formulae for relevant scattering observables like the reaction cross section. For instance, the first evidence for the large size of halo nuclei, came from the comparison between measured and calculated interaction and reaction cross section obtained within the Glauber model. The biggest limitation of such an approach is that it cannot be applied at low energy reactions which are often of interest for astrophysics. At low energy, the task of modelling reaction dynamics is more complicated because many assumptions cannot be applied any longer. A theory that can be applied at low energy and that is able to reproduce many experimental data of different observables, is CDCC. This method consists in treating the projectile as a n-body object where each of the n-constituents (which can be either individual nucleons or clusters) interacts with the target through a two-body complex effective potential. The phenomenological interaction is energy-dependent and with its parameters tuned to fit reaction data of the specific combination constituent-target. See 1.4.2 for further details. In addition to these approaches which essentially look for solutions of the time-independent Schrödinger equation, there are other semiclassical methods that solve the time-dependent Schrödinger equation assuming the relative motion between projectile and target to follow a classical trajectory [28].

In subsection 1.4.1, a short overview of main results obtained by some of the available microscopic structure models is presented while in subsection 1.4.2, the same is done concerning reaction models.

1.4.1 Nuclear structure models

A variety of microscopic structure model that aim to describe the properties of halo nuclei is available and in the following I will briefly discuss few of them highlighting some of their results.

- **No Core Shell Model (NCSM)**: the model is based on the idea to construct an effective Hamiltonian by means of a unitary transformation and to diagonalise it in terms of a large single-particle harmonic oscillator (h.o.) basis. Accurate NN interactions have short-range correlations and, in order to account for them in a truncated model space keeping the calculation feasible one has to rely on effective interactions. If on one hand side the usage of a h.o. basis allows to keep the translational invariance of the system, on the other side the resulting wave function does not exhibit the correct asymptotic behaviour. For example, this is believed to be the reason for the wrong prediction of the ground state parity of ^{11}Be in [29]. An extension of the NCSM, the *No Core Shell Model/Resonating Group Method (NCSM/RGM)*, is able to reproduce the correct spin-parity. This *ab initio* approach provides a unified description of both structure and reaction properties for light nuclei, due to the expansion of the A-body wave function onto a basis of cluster states which are described within the standard NCSM. Bound and scattering states are treated at the same time within the same approach and cluster correlations are explicitly taken into account.

  Within this approach, a relevant reaction for astrophysics has been studied: the ^{7}Be(p,γ)^{8}B radiative capture. The astrophysical S-factor was calculated and compared with experimental data: the theoretical calculation is in agreement with some sets of data but underestimates an other [30].

  The main limitation of the NCSM or NCSM/RGM approaches is that they can only be applied to light-medium mass nuclei.

- **Green Function Monte Carlo (GFMC)**: The method consists in solving stochastically the integral version of the Schrödinger equation by means of Green functions. This approach is best suited to obtain ground state wave functions for a given system system. In [31] the binding energies for the lithium and helium isotope chains were computed. Results show a very good agreement with experimental data when 3NFs are included.

The biggest limitation of this approach is that it is very time consuming and so far the largest system that can be studied has A=12 nucleons.

- **Hyperspherical Harmonics**: the method consists in rewriting the time-independent Schrödinger equation in terms of hyperspherical coordinates, hyperradius and hyperangles, which are the three-body version of the spherical coordinates. The solution is a wave function which is factorised into an hyperangular term, solution of the part of the Hamiltonian which only depends on the hyperangles, and an hyperradial wave function that is obtained solving the hyperradial Schrödinger equation. This method is completely equivalent to that used for two-body problems. It has been applied to study the ground state energy of ^{6}He [32] and its matter and charge radii [33]. The ground state energy resulted to be dependent from the cutoff used in the effective Hamiltonian while the matter radius showed a good agreement with the experimental value. The comparison between the calculated charge radius and its measured value was not good and the reason for this is thought to be due to the non inclusion of 3NF in the calculation.

  Also in this case, the limitation lies in the maximum size of the system to study.

- **Coupled Cluster (CC)**: This approach is based on the exponential ansatz for the A-body wave function of the system where the exponential of the *cluster operator* T is applied onto an uncorrelated reference wave function given in terms of a single-particle basis. The cluster operator is given as a liner expansion in particle-hole excitation amplitudes. To make the calculation feasible, the expansion of T is truncated at a given particle-hole excitation level, which in general consists in truncating it at single/double excitation level. It is a very powerful method because through the exponentiation of T, which makes the expansion non linear, higher order corrections are taken into account just considering only double excitations. With respect to other ab initio methods, the requested computing power scales more softly with an increasing size of the system and this makes it useful to approach heavier systems. A limitation of such an approach consists in the fact that it is not well suited to treat systems which exhibit an open shell structure. In [16], the ground state energies and decay width of helium isotopes were investigated: the pattern of binding energies was found to be in qualitative agreement with results of GFMC, the difference between them due to the non inclusion of 3NF in the CC calculation. Moreover, the decay widths were in semi quantitative agreement with experimental data.

- **Halo Effective Field Theory**: at low energy, where nucleons are the appropriate degrees of freedom to describe physical phenomena, QCD is non perturbative and one has to rely on effective field theories (EFT). EFT are constructed by writing down the most general Lagrangian consistent with the symmetries of the underlying theory QCD and by setting up a power counting scheme by means of which it is possible to identify the terms that mainly contribute to the calculation of a given observable. To improve the accuracy of the result, is then sufficient to add the next term according to the counting scheme. Thanks to this systematic approach, it is possible to estimate the error which is done by truncating the expansion at a given order. EFT should be applied to systems where a separation of scales is present: given Q the momentum typical of the physical problem under study and Λ the momentum at which high energy effects start to become relevant, the observables are calculated in power of $\frac{Q}{\Lambda}$. Details of short distance/high energy physics are not resolved but their effect is enclosed in the low energy coupling constants that multiply each term in the expansion.

  Halo nuclei seems to be a perfect example where EFT can be applied as they exhibit a separation of scales in terms of the size of the core R_{core} compared to that of the halo R_{halo}. In this view, the relevant degrees of freedom are the core and the valence nucleons and the expansion can be done in powers of $\frac{R_{core}}{R_{halo}}$. Halo EFT has been applied to study several processes. For example, it was used to investigate the photodissociation of ^{11}Be [34] where it was able to predict with high accuracy the strength of the transition from the bound state to the ^{10}Be+n state in the continuum. In [35] it was used to calculate the S-factor relative to the ^{7}Be(p,γ)^{8}B reaction obtaining a good comparison with experimental data.

  The advantages of studying halo nuclei within an EFT approach are that systematic improvements of calculations together with error estimates are naturally possible. Moreover, it is possible to establish relationships between observables that hold for any one-nucleon halo system so the theory possesses a universal character.

1.4.2 Nuclear reaction models

Halo nuclei cannot be studied using standard spectroscopic methods as they are too short-lived and therefore are investigated through indirect methods such as nuclear reactions. Compared to elastic scattering, knockout or transfer reactions, breakup reaction measure-

ments are especially well suited to analyse weakly bound systems. These measurements are performed sending a loosely bound projectile on a target and detecting events where the projectile breaks up. In order to extract useful information from reaction measurements data, an accurate reaction model, together with a realistic description of the projectile, is required. There is a variety of reaction models and in the following I will revise just few of them, such as the Glauber model [19], time dependent models (TD) [20], models based on the eikonal approximation [21], [22], [23] and CDCC [24].

- **Glauber model:** this theory is based on the eikonal approximation and thus can be applied to the description of high energy collisions. The reaction cross section for a given process can be computed by integrating the 'optical phase shift function' over the impact parameter. This function is defined as the matrix element of the multiple-scattering operator, taken between a product of the projectile and target wave functions. It is non trivial to compute such a matrix element because the multiple-scattering operator is an A-body operator. Approximations need to be done, by substituting the wave functions with densities and assuming these densities to be products of one-body densities, or by expanding the multiple-scattering operator as a sum of two-body, three-body,...operators and truncating it at a given order. In general, the most used one is the 'optical limit approximation', where one-body densities are employed and the A-body multiple-scattering operator is replaced by a two-body operator. Attempts have been done to include contributions from higher order terms in the expansion of the multiple-scattering operator because the optical limit approximation is not enough to get quantitative results, especially for halo nuclei (see [36] where this was pointed out in the case of the reaction cross section of ^{11}Li). By using one-body densities, correlation effects are not included in the calculation even if all the terms in the multiple-scattering operator expansion would be considered. A solution to this issue consists in evaluating each term of the expansion analytically, provided that certain conditions are fulfilled. This method has been applied to nucleus nucleus scattering as in [37], where the reaction cross section was calculated for reactions involving various combinations of ^{4}He, ^{6}He, ^{9}Be, ^{12}C and ^{27}Al and the agreement with experimental data was found to be better with respect to calculations performed within the optical limit approximation. But such an approach cannot be always applied: the number of terms in the expansion becomes very large for heavier system and if some conditions are not fulfilled, the analytical evaluation of the integrals cannot be done. In Ref. [38], a different approach was proposed: to use

Monte Carlo integration to evaluate the matrix element of the multiple-scattering operator. This method has the advantages that sophisticated wave functions for the projectile and target can be used and that the multiple-scattering operator can be treated fully without making use of any expansion nor truncation. They calculated reaction and elastic differential cross section for different combinations such as proton-nucleus (p-^{6}He) and nucleus-nucleus (^{6}He-^{12}C). Reaction cross section for p-^{6}He and p-^{6}Li were calculated within the optical limit approximation and within the Monte Carlo approach: the comparison showed that the results of the optical limit approximation are smaller than the others. Calculations of the elastic differential cross sections again for p-^{6}He,^{6}Li underestimate the experimental data.

- **Time dependent models**: the key idea is to solve numerically the time dependent Schrödinger equation assuming that the projectile-target relative motion can be approximated by a classical trajectory and making use of a few-body description of the projectile as a structureless core to which one or two valence nucleons are weakly bound. The binding potential is in general a simple, local potential tuned to reproduce the projectile bound states. There are several techniques to solve the time dependent Schrödinger equation ([39], [40], in [41] a mutipole expansion of the projectile-target potential is employed as well as some perturbation theory approximations to reach faster convergence), but I will follow [20] as an example. In that study, they are interested in calculating the breakup cross section of ^{11}Be to test the accuracy of a few-body description of the projectile as well as the sensitivity of the calculations to the parametrization of the binding potential. In the rest frame of the projectile, the target moves along a classical trajectory and thus the interaction between projectile and target is described by a time dependent potential; the internal motion of the projectile is treated quantumechanically by solving a time dependent Schrödinger equation with the initial condition that the projectile is in its ground state. The projectile wave function is then solved iteratively using an algorithm described in [42]. The calculation is repeated for different trajectories which are distinguished by different values for the impact parameter. They tested the nuclear induced breakup of ^{11}Be on ^{12}C and found it very sensitive to the choice of optical potential between projectile and target leading to variations in the magnitude of the breakup cross section (although the pattern remained unchanged). In order to improve accuracy of the calculation and thus the quality of the theoretical predictions, a better description of the projectile, which goes beyond the few-body

model, should be used.

- **Eikonal-CDCC and Dynamical Eikonal approximation**: the Eikonal-CDCC method (ECDCC) is a variation of the ordinary CDCC method which makes use of the eikonal approximation and is thus reliable to describe reactions occurring at high energy. In [21] the formalism of the ECDCC method is reviewed. As in standard CDCC, the projectile is described as a two-body object made of a core and a valence nucleon and the wave function describing the system is expanded onto the eigenfunctions of the internal Hamiltonian which describes the projectile only. The difference with respect to ordinary CDCC is that the incident plane wave for the projectile-target relative motion is factorised out of the three-body wave function as the eikonal approximation assumes that the total wave function does not vary significantly from a plane wave. Then, the coupled channels equations to be solved are much simpler than those of CDCC. Using the eikonal approximation reduces the computationl time required by ordinary CDCC. Corrections can be done by replacing the partial scattering amplitudes for small projectile-target orbital angular momentum L with those obtained from a standard CDCC calculation; this approach is still faster than CDCC although it keeps the same level of accuracy. In [43], the ECDCC method together with corrections is developed and applied to the test case of the breakup of ^{8}B on a ^{58}Ni target. This version of ECDCC is based on the idea of decomposing the scattering amplitude into low-L contributions, which are calculated within CDCC, and high-L terms which are obtained from ECDCC. For reactions at intermediate energies, a relativistic treatment of the breakup process has to be performed. In the past this was done by modifying the kinematics factors only, while in [44], a proper relativistic treatment of the dynamics of the reaction is incorporated in the ECDCC method, using a relativistic version for the interaction potential between projectile and target. The most accurate version of ECDD seems thus to be that were, for small L the non relativistic CDCC partial scattering amplitudes are used, while at large L, the relativistic ECDD ones are employed. In this way, quantum mechanical and relativistic corrections are considered keeping the advantage of the simplicity when performing a calculation based on ECDDD.

  The Dynamical Eikonal (DEA) approximation [22], [23], is a method based on the eikonal approximation but that, differently from most of the other model based on the eikonal approximation, does not rely on the adiabatic approximation as well. The adiabatic approximation assumes that the projectile internal motion varies more slowly

than its center of mass motion. The internal degrees of freedom of the projectile are seen as 'frozen' during the time when the collision with the target occurs. The key idea is that to expand the wave function of the system on a three-dimensional mesh without employing the partial wave expansion of CDCC. It thus describes bound and continuum states of the projectile on the same footing with no need for a continuum discretization as CDCC. Since the three-body dynamics is explicitly treated, coupled channels effects are automatically included. The equation that needs to be solved is formally equal to a time dependent Schrödinger equation, that is solved for each value of the impact parameter assuming a constant projectile-target relative velocity. Since DEA explicitly includes the internal Hamiltonian of the projectile in the equation, it treats the change in eigenenergy of the projectile during the collision. The fact that the relative velocity is not changed accordingly, introduces a violation of the total energy conservation but its effect is considered to be negligible. At low energy the DEA is not reliable because the eikonal approximation does not hold anymore and the Coulomb interaction produces a distortion of the projectile-target relative motion from the plane wave. The method was tested for one-neutron halo projectile colliding on light and heavy target at high energies and the agreement with experimental data was very good.

In [45], a comparison between DEA and ECDCC calculations for the breakup cross section of ^{15}C on ^{208}Pb showed that the two methods provide the same results when the Coulomb interaction is artificially switched off. When the Coulomb interaction is present, the two methods provide different results and none of them agrees with CDCC. However, it is possible to apply a correction to both and in the case of ECDCC, the final result agrees much better with that of CDCC showing that the lack of the Coulomb deflection can be corrected.

The two methods based on the eikonal approximation are able to provide accurate results within the energy range of their applicability keeping the computational time short compared to CDCC. The hybrid version of ECDCC with quantum corrections leads to a model that exhibits the same accuracy as the full CDCC, allowing to describe Coulomb and nuclear induced breakup reactions in a wide range of incident energies with a minimal computational cost.

Among the reaction models, CDCC is one of those which provides results in very good agreement with experimental data for a wide range of reactions over a broad spectrum of

energies. I will now devote special attention revising the method because I will compare my results with those obtained by a CDCC calculation. In the following, I will briefly revise the key concepts upon which the method is based through one example: the fusion reaction of ^{11}Be on ^{208}Pb [46].

The halo projectile is described as a ^{10}Be core with a valence neutron orbiting around it. The three-body system, target + ^{10}Be core +n, is described in terms of two degrees of freedom, $\vec{R}$ and $\vec{r}$, which represent the distances between the centre of mass of the projectile and target and that between the core and valence neutron respectively. The system is governed by the Hamiltonian:

$$H = T_R + V_{ct}(\vec{R} + \frac{A_n}{A_p}\vec{r}) + V_{nt}(\vec{R} - \frac{A_c}{A_p}\vec{r}) + h(\vec{r}), \tag{1.1}$$

where T_R is the kinetic energy operator of the projectile-target relative motion, V_{ct} and V_{nt} are the interaction potentials between core-target and neutron-target respectively and $h(\vec{r})$ is the Hamiltonian which describes the projectile:

$$h = T_r + V_{cn}(\vec{r}). \tag{1.2}$$

Here T_r is the kinetic energy operator of the projectile and V_{cv} the binding potential between core and neutron.

The wave function of the three-body system is expanded onto a basis set of eigenstates ϕ_i of $h(\vec{r})$ and reads:

$$\Psi(\vec{R},\vec{r}) = \phi_0(\vec{r})\,\chi_0(\vec{R}) + \sum_{n>0}\phi_n(\vec{r})\chi_n(\vec{R}). \tag{1.3}$$

The first term is the product between the projectile ground state wave function ϕ_0 and the incoming plane wave χ_0 describing the projectile-target relative motion. The second term is a sum over all the possible projectile excited states ϕ_n, and projectile-target relative motion wave function χ_n with the projectile in a given excited state. The excited states of the projectile can be either bound or in the continuum: for each value of the projectile orbital angular momentum l, a maximum value of excitation energy ϵ_{max} is chosen and the interval $[0-\epsilon_{max}]$ is discretized in bins. For each bin, a wave function is constructed as:

$$\phi_{(ls)j,[k_1,k_2]}(r) = \sqrt{\frac{2}{\pi\,N}}\int_{k_1}^{k_2} w(k)e^{-i\delta_k}u_{(ls)j,k}(r)dk \tag{1.4}$$

where N is a normalization constant, $[k_1,k_2]$ is the width of the energy bin, $w(k)$ is a weight function and δ_k is the scattering phase shift for the scattering wave function $u_{(ls)j,k}(r)$. Here

j is the projectile total angular momentum obtained by the coupling of the orbital angular momentum of the core relative to the neutron with the spin of the neutron s (the core is regarded as spinless). The projectile ground state wave function and the scattering states are solution of the Schrödinger equation with the $V_{cn}(\vec{r})$ potential.

To obtain the projectile-target relative motion radial wave function $\chi_{\alpha J}$, this set of coupled equations is solved for each value of total angular momentum J:

$$\left[-\frac{\hbar^2}{2\mu}\left(\frac{d^2}{dR^2}-\frac{L(L+1)}{R^2}\right)-E+\epsilon_\alpha+V^J_{\alpha,\alpha}(R)+iW_F(R)\right]\chi_{\alpha J}(R)=\sum_{\alpha,\alpha'} i^{L'-L}V^J_{\alpha,\alpha'}(R)\chi_{\alpha' J}(R) \tag{1.5}$$

where $\alpha = L, l, s, j, n$ represents a set of quantum numbers with L being the orbital angular momentum of the projectile relative to the target. The quantity $V^J_{\alpha,\alpha'}$ represents the coupling potential between the states labeled with quantum numbers (α, α') as:

$$V^J_{\alpha,\alpha'}(\vec{R}) = \langle\phi_\alpha(\vec{r})|V_{ct}(\vec{R}+\frac{A_n}{A_p}\vec{r})+V_{nt}(\vec{R}-\frac{A_c}{A_p}\vec{r})|\phi_{\alpha'}(\vec{r})\rangle. \tag{1.6}$$

The operator $W_F(R)$ is an imaginary short-ranged potential which is defined in terms of the distance between the center of mass of the projectile with respect to the target. This operator is added to the Hamiltonian of equation (1.1) in order to simulate fusion and can be regarded as an absorber which removes flux from the entrance channel taking into account the irreversible character of fusion. The total fusion cross section is defined in terms of the flux which leaves the elastic scattering channel. It includes both the contributions from incomplete and complete fusion events, which are the processes where either only part of the projectile's constituents or the whole projectile are fused with the target. In this work, the complete fusion cross section is defined as the absorption cross section from only bound states of the projectile and the capture from continuum states is not included because it cannot be distinguished from the capture of just one projectile's constituent. The incomplete fusion is then regarded as the absorption from breakup channels.

Total and incomplete fusion cross sections were calculated including or neglecting the couplings between continuum states. The results of this work showed that continuum continuum couplings affect significantly the fusion dynamics, they tend to suppress all the fusion processes as they remove flux that could penetrate the Coulomb barrier.

Chapter 2

Methodology

When a halo nucleus interacts with a target, due to the high probability for such a weakly-bound projectile to dissociate, at a given incident energy several reaction paths are simultaneously allowed as shown in Fig. 2.0.1.

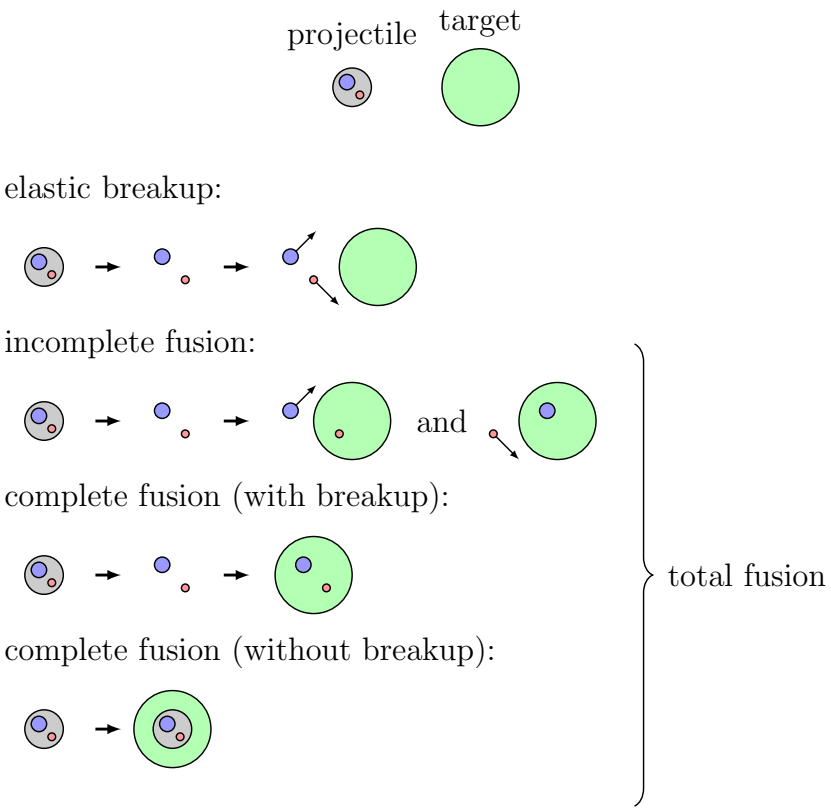

Figure 2.0.1: Some of the reaction processes in low-energy collisions of weakly-bound nuclei with stable targets.

These can be grouped in two main categories: events where none of the projectile constituents are captured by the target, called *no capture break-up* (NCBU), and events associated with fusion. Among these, it is possible to distinguish further between the case where only a part of the fragments is captured, *incomplete fusion* (ICF), and the case where

the projectile fully fuses with the target, *complete fusion* (CF). Two different processes contribute to the CF event: one where the projectile breaks up and all its constituents are captured by the target, and one where it fuses with the target as a whole without a preceding break up. The focus of this study is that to understand how the projectile internal structure, which is reflected in its break up probability, affects the fusion processes. The difficulty lies in building a quantum theory able to provide a quantitative description for each individual process independently one from the other still within a unified picture.

In this section, the theoretical concepts on which the method is based, are presented within a model where the projectile is thought as made up on two constituents and the target has no internal structure. This three-body model addresses the problem from a time-dependent point of view, allowing to follow the evolution of the collision with time. In this way, it is possible to construct a picture of what is happening at any desired moment facilitating the understanding of how the reaction observables arise during the collision. The method consists of four main steps:

(i) to construct the three body wave function $\Psi(t = 0)$ describing the system at the initial time,

(ii) to propagate $\Psi(0) \rightarrow \Psi(t)$, where the propagation is governed by the time evolution operator, $\exp(-\frac{\mathrm{i}}{\hbar}\hat{\mathcal{H}}t)$, with $\hat{\mathcal{H}}$ being the total Hamiltonian of the system,

(iii) to calculate relevant observables using the wave function $\Psi(t_f)$, where t_f is the time when a stationary regime is reached.

(iv) to extract the energy dependence of observables.

2.1 One dimensional model

I first approached the problem developing a one-dimensional model. All the nuclei lie on a line in coordinate space and the system in the overall center of mass is described in terms of two degrees of freedom : R and ξ. These represent the distance between the target and the center of mass of the projectile and the distance between the two projectile constituents respectively. Figure 2.1.1 shows the system of coordinates including the distances between the target and each of the two fragments, x_1 and x_2. Later I extended the model to three dimensions: the theoretical concepts remained the same with the angular degrees of freedom being the only element which had to be introduced.

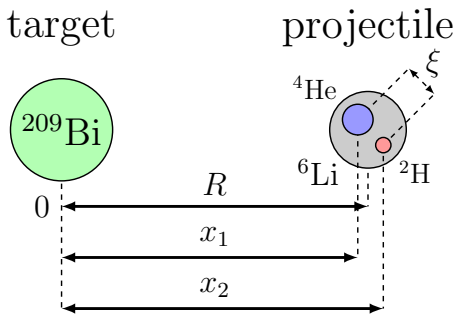

Figure 2.1.1: System of coordinates for the one-dimensional model.

I started with the implementation of the one-dimensional model in a Fortran 90 code which later I could expand to incorporate the changes needed to perform calculations in three dimensions. Since the basic ideas behind it are the same of the three-dimensional version just simplified by the absence of angular degrees of freedom, in the following I will directly describe the methodology of the three-dimensional version.

2.2 Three-dimensional model: choice of the reference frame

The ^{6}Li + ^{209}Bi collision is used as a test case and is investigated within a one and three-dimensional model. The reference frame is chosen to be one which rotates together with the system with respect to the Cartesian overall center of mass frame that has its axis fixed and parallel to those of the laboratory frame. Not only it provides a more natural way to study the problem when the system is invariant under rotations, but it also is more computationally efficient. In [47], the wave packet method for the inelastic scattering of an atom off a diatom was presented in a body-fixed (BF) representation. The speed of the calculations was analysed in terms of the computational cost needed to propagate the coupled wave packets and compared to the performance of the same method when employing a space fixed reference frame. It was found that for a large number of states N, the BF calculations scale as $\sim N^{3/2}$ which is more efficient than a space fixed calculation which scales as $\sim N^2$. As it was pointed out in [48], the simplest approach to perform a quantum dynamical calculation for a three body system consists in working in a Cartesian coordinate representation employing two Jacobi vectors that describe the translationally invariant configuration space. The problem is that the implementation of the action of

the Hamiltonian on the wave function within this approach turns out to be numerically inefficient. The solution consists in finding a coordinate representation that would be more computationally efficient. Considering the rotational symmetry of the problem, the best choice is that of embedding in the system an axis frame which defines a reference frame that rotates with the system in a given way. The BF frame is then related to the original SF frame through an orthogonal transformation which describes the rotational motion of the system with respect to the space fixed frame. This transformation is parametrized by three variables, the Euler angles, while the remaining 3A-6 degrees of freedom describe the rest of the motion and are referred to as *internal coordinates*. The choice of the internal coordinates, as that of the particular rotation of the system, is not unique; in this work I follow that described in [49]. In this work, Tennyson and Sutcliffe derive the expression for the three dimensional Hamiltonian in the BF frame for an atom-diatom system and then apply the formalism to study the vibrational spectrum and ground state energy of KCN.

The BF frame is constructed embedding an axis frame in the system and defining a coordinate transformation that relates the BF frame with the original space fixed frame. The three body system is initially described in a translationally invariant space fixed frame through a pair of Jacobi vectors $\bar{t}_1$ and $\bar{t}_2$. The first vector $\mathrm{In}\bar{t}_1$ is associated with the distance between the center of mass of two bodies and the third, $\bar{t}_2$ with the distance between the two bodies whose center of mass was taken as reference in the definition of $\bar{t}_1$. The two Jacobi vectors correspond to the vectors $\bar{z}_1$ and $\bar{z}_2$ expressed in the BF frame, provided that

$$t_i = C z_i, \tag{2.1}$$

where C is the orthogonal matrix which only depends on the Euler angles and which describes the rotation of the BF frame with respect to the original frame. In references [49], [50], and in the present work, the orientation of the BF frame is such that the new axes are the unit vectors of $\bar{t}_1$ in spherical coordinates so that the new z-axis lies along $\bar{t}_1$ and the new y-axis is left in the original $x - y$ plane. The three missing degrees of freedom are the internal coordinates which are chosen to be the lengths R and ξ of $\bar{t}_1$ and $\bar{t}_2$ respectively, and the angle θ between them ranging from $(0, \pi)$. It is important to notice that in principle many other embeddings are possible. Figure 2.2.1 shows the relation between space- and body-fixed reference frames.

The Hamiltonian of the system in the Cartesian, translationally invariant space-fixed

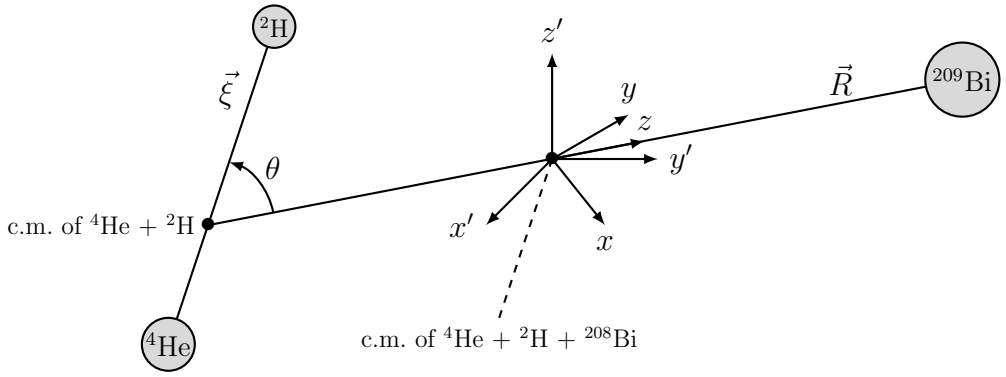

Figure 2.2.1: Reference frame and coordinates employed to describe the system. The primed axis represent the Cartesian translationally invariant space fixed reference frame while the unprimed ones represent the particular choice of the reference frame fixed with the bodies. The coordinate $R = \|\vec{R}\|$ denotes the distance between the target and the center of mass of the projectile, $\xi = \|\vec{\xi}\|$ is the distance between the constituents of the projectile and θ is the angle between $\vec{R}$ and $\vec{\xi}$.

frame is given by:

$$\hat{\mathcal{H}} = -\frac{\hbar^2}{2\mu_{\mathrm{TP}}}\nabla^2(t_1) - \frac{\hbar^2}{2\mu_{12}}\nabla^2(t_2) + U(|\bar{t}_2 - \bar{t}_1|) + V(\bar{t}_1, \bar{t}_2), \tag{2.2}$$

where $\mu_{\mathrm{TP}} = M(m_1 + m_2)/(M + m_1 + m_2)$ is the reduced mass of the target (M) and projectile, with constituent masses m_1 and m_2; $\mu_{12} = m_1 m_2/(m_1 + m_2)$ is the reduced mass of the projectile constituents. The potential U binds the projectile constituents together and V is the sum of the interaction potentials between the target and the projectile constituents. For each binary system, including ^{4}He–^{2}H, the potential V is the sum of the Coulomb and nuclear interactions. The Coulomb potential of a uniformly charged sphere was used:

$$V_{\mathrm{C}}(r_i) = \begin{cases} \frac{Z_i Z_{\mathrm{T}}}{4\pi\epsilon_0}\frac{1}{r_i} & \text{if } r_i > R_{\mathrm{T}} \\ \frac{Z_i Z_{\mathrm{T}}}{4\pi\epsilon_0}\left(\frac{3}{2R_{\mathrm{T}}^2} - \frac{r_i^2}{2R_{\mathrm{T}}^3}\right) & \text{if } r_i \leq R_{\mathrm{T}} \end{cases} \tag{2.3}$$

where Z_i is the electric charge of the fragment i, Z_{T} is the electric charge of the target and R_{T} is the target radius defined as $R_{\mathrm{T}} = r_{0c}A_{\mathrm{T}}^{1/3}$. The nuclear potentials have the Woods–Saxon form:

$$V_{\mathrm{WS}}(r_i) = \frac{V_{0i}}{1 + \exp\left(\frac{r_i - \mathrm{r}_{00i}}{\mathrm{a}_{0i}}\right)}. \tag{2.4}$$

where the critical distances r_{00i} are determined by $r_0 A^{1/3}$, where A is the heaviest mass for the corresponding binary system. The parameters of the Woods–Saxon potentials (2.4) for

all binary systems are given in Table 2.2.1. The choice for the parameters was done in order to have values of the Coulomb barriers similar to the Sao-Paolo potential barriers [51]. The values of the Coulomb barriers for the two binary systems are given in the last column of Table 2.2.1.

Table 2.2.1: Parameters of the Woods–Saxon nuclear potentials used in the present calculations, together with the radius parameters of the Coulomb potentials of a uniformly charged sphere.

system	V_0 (MeV)	r_0 (fm)	a_0 (fm)	r_{0c} (fm)	V_B (MeV)
^{209}Bi-^{4}He	-32.9313	1.4610	0.6050	1.2	21.24
^{209}Bi-^{2}H	-26.0000	1.4650	0.6680	1.2	10.04
^{4}He+^{2}H	-78.4600	1.1500	0.7000	1.465	

The transformation of the Hamiltonian (2.2) into the BF frame is tedious and complicated. Here I will only report the final result while the details of the a derivation can be found in Appendix A of Ref. [49] or in [52]. The Hamiltonian (2.2) expressed in the BF frame becomes:

$$\hat{\mathcal{H}} = \hat{\mathcal{H}}_1 + \hat{\mathcal{H}}_2 + V(R,\xi,\theta) + U(\xi) \tag{2.5}$$

where:

$$\begin{aligned}\hat{\mathcal{H}}_1 = &-\frac{\hbar^2}{2\mu_{TP}R^2}\frac{\partial}{\partial R}\left(R^2\frac{\partial}{\partial R}\right) - \frac{\hbar^2}{2\mu_{12}\xi^2}\frac{\partial}{\partial \xi}\left(\xi^2\frac{\partial}{\partial \xi}\right)\\ &- \frac{\hbar^2}{2}\left(\frac{1}{\mu_{TP}R^2}+\frac{1}{\mu_{12}\xi^2}\right)\frac{1}{\sin\theta}\frac{\partial}{\partial\theta}\left(\sin\theta\,\frac{\partial}{\partial\theta}\right)\end{aligned} \tag{2.6}$$

$$\begin{aligned}\hat{\mathcal{H}}_2 = \frac{1}{2}\Bigg[&\frac{1}{\mu_{TP}R^2}\left(\hat{J}^2-\hat{J}_z^2\right)+\left(\frac{\cot^2\theta}{\mu_{TP}R^2}+\frac{\csc^2\theta}{\mu_{12}\xi^2}\right)\hat{J}_z^2\\ &+\frac{\cot\theta}{\mu_{TP}R^2}(\hat{J}_x\hat{J}_z+\hat{J}_z\hat{J}_x)\Bigg]+\frac{\hbar}{\mathrm{i}}\frac{1}{\mu_{TP}R^2}\left(\frac{\partial}{\partial\theta}+\frac{\cot\theta}{2}\right)\hat{J}_y\end{aligned} \tag{2.7}$$

where J_i are the component of the total angular momentum operator of the system in the BF frame.

Since the total angular momentum J is conserved one can consider individual J-components Ψ^J of the total wave function. Each of the components, is an eigenfunction of the Hamiltonian of Eq. (2.5) and can be written as a sum of products between functions depending on the internal coordinates and rotational eigenfunctions:

$$\Psi^J = \sum_{K=-J}^{J} \Psi^{JK}(R,\xi,\theta)\mathcal{D}^J_{m0K}, \tag{2.8}$$

where $\mathcal{D}^J_{m0K}$ is an element of the Wigner D-matrix with $m0$ the eigenvalue of the z component of the total angular momentum of the projectile and is a function of the Euler angles only. The quantum number K is the eigenvalue of the J_z component of the total angular momentum in the BF frame. If the action of the Hamiltonian (2.5) on the wave function of (2.8) is calculated, the result is multiplied from the left by $\mathcal{D}^{J*}_{m0K'}$ and integrated over the Euler angles, the final result is an effective Hamiltonian that is used to determine Ψ^{JK}. Details of the derivation of this effective Hamiltonian can be found in Appendix A and only the result is stated here:

$$\hat{\mathcal{H}}^J_{\text{eff}} = \hat{\mathcal{H}}^J_{KK} + \hat{\mathcal{H}}^J_{KK+1} + \hat{\mathcal{H}}^J_{KK-1} \tag{2.9}$$

where:

$$\begin{aligned}\hat{\mathcal{H}}^J_{KK} = &-\frac{\hbar^2}{2\mu_{TP}}\frac{\partial^2}{\partial R^2} - \frac{\hbar^2}{2\mu_{12}}\frac{\partial^2}{\partial \xi^2} + \frac{\hbar^2 \hat{j}^2_\xi}{2\mu_{12}\xi^2} \\ &+ \frac{\hbar^2[J(J+1) - 2K^2 + \hat{j}^2_\xi]}{2\mu_{TP}R^2} + V(R,\xi,\theta) + U(\xi)\end{aligned} \tag{2.10}$$

and

$$\hat{\mathcal{H}}^J_{KK\pm1} = -\frac{\hbar^2}{2\mu_{TP}R^2}\sqrt{J(J+1) - K(K\pm1)}\hat{j}_\mp. \tag{2.11}$$

The operator $\hat{j}_\xi$ is the total angular momentum of the projectile defined as:

$$\hat{j}^2_\xi = -\left(\frac{1}{\sin\theta}\frac{\partial}{\partial\theta}\sin\theta\frac{\partial}{\partial\theta} - \frac{K^2}{\sin^2\theta}\right) \tag{2.12}$$

and

$$\hat{j}_\pm = \mp\frac{\partial}{\partial\theta} - K\cot\theta. \tag{2.13}$$

The operator $\hat{j}^2_\xi$ in Eq. (2.12) is left in operator form since it is not a good quantum number because it is not conserved on its own, but only when combined with the orbital angular momentum of the target relative to the projectile. Transition from $\mathcal{H}$ in Eq. (2.5) to $\mathcal{H}^J_{\text{eff}}$ in Eq. (2.9) is accompanied by redefinition of the wave function $R\xi\Psi^{JK}(R,\xi,\theta) \to \Psi^{JK}(R,\xi,\theta)$. Thus, the normalization condition becomes:

$$\int |\Psi^{JK}(R,\xi,\theta)|^2 dR d\xi d\theta = 1. \tag{2.14}$$

The time-dependent Schrödinger equation that has to be solved is:

$$\mathrm{i}\hbar\frac{\mathrm{d}}{\mathrm{d}t}\Psi^{JK} = \hat{\mathcal{H}}^J_{KK}\Psi^{JK} + \hat{\mathcal{H}}^J_{KK+1}\Psi^{JK+1} + \hat{\mathcal{H}}^J_{KK-1}\Psi^{JK-1}. \tag{2.15}$$

From Eq. (2.15) it is possible to see that states with different K values are coupled together through the coupling terms $\hat{\mathcal{H}}^J_{KK\pm1}$ which are known as *Coriolis coupling* (see Appendix C).

2.3 Preparation of the initial state

At the initial time t_0, if the projectile is located far away from the target that the mean value of the interacting potential $\langle\Psi(t_0)|V(R,\xi,\theta)|\Psi(t_0)\rangle$ is negligible the Hamiltonian is separable. Consequently, the initial wave function of the system can be written as a product of three functions, each of them depending only on one of the internal coordinates:

$$\Psi^{JK}(R,\xi,\theta,t=t_0)=\Phi_0(R)\chi_0(\xi)\phi_0(\theta,K), \tag{2.16}$$

where $\Phi_0(R)$ is a Gaussian wave packet centered around R_0 with spatial width σ and initial wavenumber $P_{R0}/\hbar$:

$$\Phi_0(R)=\frac{1}{\pi^{1/4}\sqrt{\sigma}}\exp\left[-\frac{(R-R_0)^2}{2\sigma^2}\right]\exp\left[-\frac{\mathrm{i}}{\hbar}P_{R0}\,(R-R_0)\right] \tag{2.17}$$

The value of R_0 is chosen by calculating the expectation value of the interaction potential for different values of R_0 and then selecting the one which provides the smallest result. The larger the R_0, the smaller the mean value of V but attention is given also not to put the wave packet too close to the border of the numerical grid in the R coordinate. The algorithm that calculates the discrete Fourier transform of the wave function treats the input data as if they were periodic in the coordinate on which it acts. This means

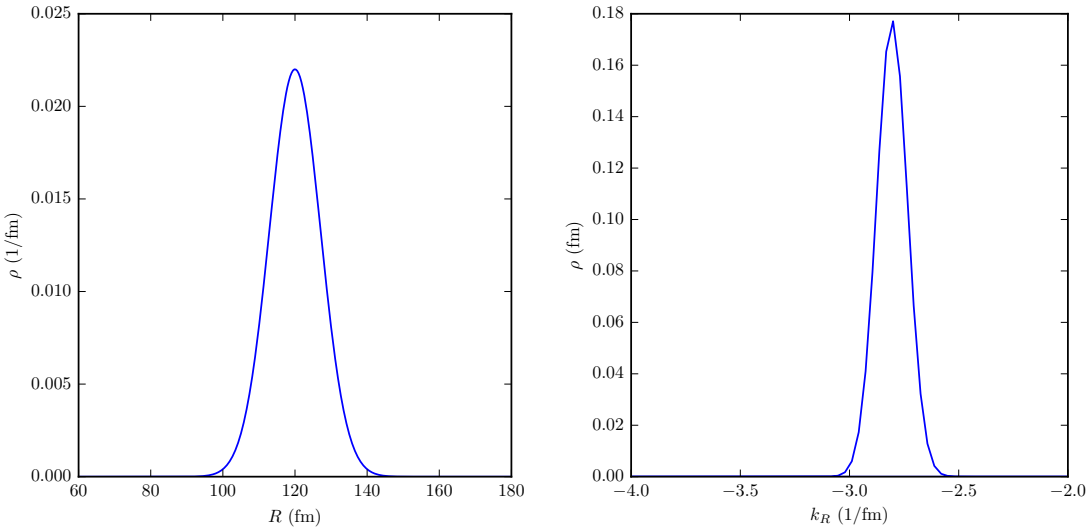

Figure 2.3.1: Density distribution ρ of the initial wave function integrated over ξ and θ as a function of the R coordinate (left panel); together with the corresponding distribution in momentum space as a function the conjugate momentum k_R (right panel).

that if the amplitude of the wave function at one grid border is different from zero it will automatically appear at the opposite side of the grid leading to unphysical results. Figure 2.3.1 (left panel) shows the density of probability of the initial wave function projected onto the R coordinate space. The dependency on ξ and θ was integrated out to show only the R-dependence. The total angular momentum J and its z-projection K are both zero. As it can be seen, the density has a Gaussian distribution with spatial width $\sigma = 10$ fm, centered around $R_0 = 120$ fm which, for a grid that covers the range $[0, 200]$ fm, seems to be a good choice to keep the expectation value of V small but without having large values at the grid border (the tail of the density goes to zero already around $R \approx 150$ fm). In the left pane of Fig. 2.3.1 the corresponding density of probability of the initial wave function in momentum space is shown as a function of the conjugate momentum k_R. The distribution is centered around negative values of momenta since the initial wave packet is travelling from right to left towards the target at $R = 0$. In Eq. (2.16), $\chi_0(\xi)$ is the ground state wave function of the pseudo-^{6}Li projectile (=^{4}He+^{2}H). It is obtained as a solution

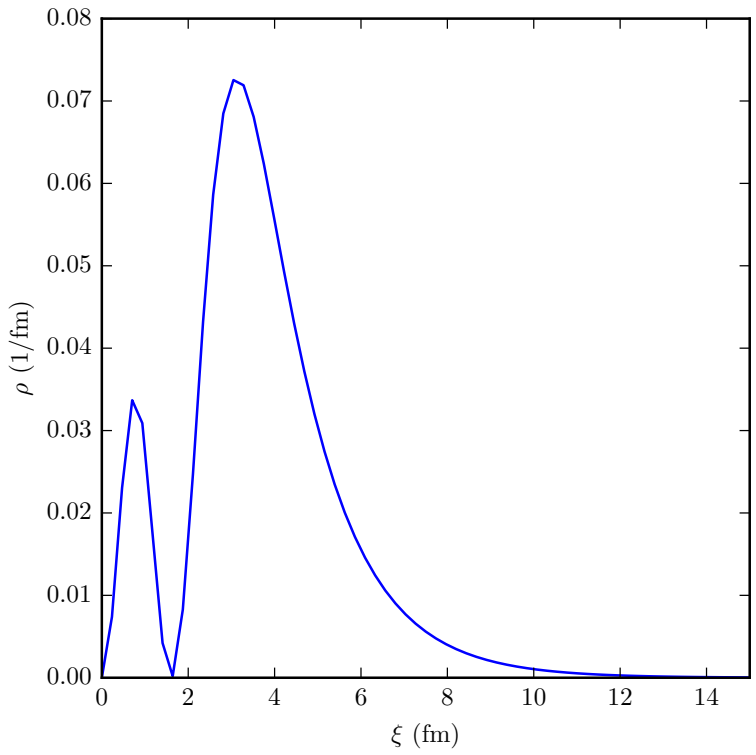

Figure 2.3.2: Profile of the density of probability as a function of the ξ coordinate at the initial time t_0. It describes the ground state density of the ^{6}Li projectile.

of the eigenvalue problem with the part of the Hamiltonian of Eq. (2.10) and (2.11) which depends only on the ξ coordinate. The wave function is calculated using a nuclear Woods-Saxon potential between the alpha particle and the deuteron and its parameters are shown in Table 2.2.1. It provides a $1s$-state with energy -1.47 MeV and it is assumed that the strongly bound $0s$-state (-32.96 MeV) is occupied by the ^{4}He nucleons. Details of the solution are presented in Appendix D. Fig. 2.3.2 shows the probability density of the wave function projected onto the ξ coordinate. Finally, the function $\phi_0(\theta, K)$ is the angular part of the ground state wave function of the projectile:

$$\phi_0(\theta, K) = P_{j0}^{m0}(\cos\theta)\delta_{K,m_0}\sqrt{\frac{2j_0+1}{2}\frac{(j_0-m_0)!}{(j_0+m_0)!}}, \tag{2.18}$$

where j_0 is the initial value of the total angular momentum of the projectile, m_0 is the initial value of its z-projection and P_{j0}^{m0} is the associated Legendre function.

2.4 Time propagation

Once the initial wave function $\Psi(t=0)$ has been constructed it is possible to solve the time-dependent Schrödinger equation. The formal solution at time $t+\Delta t$ reads:

$$\Psi(t+\Delta t) = \exp\left(-\frac{\mathrm{i}}{\hbar}\hat{\mathcal{H}}\Delta t\right)\Psi(t). \tag{2.19}$$

The time evolution operator is represented as a convergent series of Chebychev polynomials Q_n [53]:

$$\exp\left(-\frac{\mathrm{i}}{\hbar}\hat{\mathcal{H}}\Delta t\right) \approx \sum_{n=0}^{N_{\mathrm{MAX}}} a_n Q_n(\hat{H}_{\mathrm{norm}}). \tag{2.20}$$

In Eq. (2.20), the time-independent Hamiltonian is renormalised in order for its spectral range to be within the interval [-1,1], which is the domain of the polynomials, by defining

$$\hat{H}_{\mathrm{norm}} = \frac{\bar{H}\,\hat{1} - \hat{H}}{\Delta H} \tag{2.21}$$

where $\bar{H} = (\lambda_{\max} + \lambda_{\min})/2$, $\Delta H = (\lambda_{\max} - \lambda_{\min})/2$, $\lambda_{\max}$ and $\lambda_{\min}$ are respectively the largest and smallest eigenvalues in the spectrum of $\hat{\mathcal{H}}$ supported by the numerical grid, and $\hat{1}$ denotes the identity operator. The expansion coefficients in Eq. (2.20) read:

$$a_n = \mathrm{i}^n(2-\delta_{n0})\exp\left(-\frac{\mathrm{i}}{\hbar}\bar{H}\Delta t\right)J_n\left(\frac{\Delta H\,\Delta t}{\hbar}\right) \tag{2.22}$$

where J_n are Bessel functions of the first kind. Since J_n exponentially goes to zero with increasing n for $n > x$, the expansion in Eq. (2.20) converges exponentially for $n > \Delta H \Delta t/\hbar$. This representation of the time evolution operator requires the computation of the action of $Q_n(\hat{H}_{\rm norm})$ on the wave function $\Psi(t)$. The Q_n polynomials obey the recurrence relations:

$$Q_{n-1}(\hat{H}_{\rm norm}) + Q_{n+1}(\hat{H}_{\rm norm}) - 2\hat{H}_{\rm norm}Q_n(\hat{H}_{\rm norm}) = 0 \tag{2.23}$$

with the initial conditions $Q_0(\hat{H}_{\rm norm}) = \hat{1}$ and $Q_1(\hat{H}_{\rm norm}) = \hat{H}_{\rm norm}$.

This work focuses on the study of the fusion processes: within this model, fusion occurs when the projectile, or part of it, tunnels through the Coulomb barrier. Although in reality other processes as well can happen, I assume that an object which tunnelled through the barrier fused with the target. In order to simulate the irreversibility of fusion, the transmitted flux has to be permanently removed from the total incident flux. For each of the two fragments, an imaginary potential $\hat{W}_{Ti}$ is added to the Hamiltonian. Following [53], these are given by:

$$\hat{W}_{Tj} = \Delta H[\cos\delta(1 - \cosh\hat{\gamma}_j) - \mathrm{i}\sin\delta\sinh\hat{\gamma}_j] \tag{2.24}$$

where $\delta = \arccos(\frac{E-\bar{H}}{\Delta H})$, E denotes the incident energy, j= $1, 2$ identifies the projectile fragment and γ_j is a function of the coordinates which gives rise to the damping factor that is responsible for removing the transmitted flux from the entrance channel if x_1 and x_2 are smaller than the location of the Coulomb barriers RCB_1 and RCB_2. To construct W_i, the Woods–Saxon potential was used:

$$W_i(x_i) = -\mathrm{i}\frac{|\,W_{0i}|}{1 + \exp\frac{x_i - x_{0i}}{\mathrm{a}_{0i}}} \tag{2.25}$$

the depth W_{0i} and diffusiveness a_{0i} parameters are the same for W_1 and W_2, where the 1,2 stand for projectile constituents 1 and 2. What differs is the location of the complex potentials on the grid because the two constituents have different Coulomb barrier locations. The only restriction concerning the geometry of W_i is that it should act only inside the barrier. Figure 2.4.1 shows the location of W_i with respect to the total interaction constituent–target V_i, for both the constituents. The potentials W_i are zero outside the Coulomb barrier and are placed in correspondence with the local minimum of the interacting potentials V_i.

The parameters used to construct W_1 and W_2 are given in Table 2.4.1. This approach is commonly used in coupled-channels calculations and the parameters are taken from References [46] and [54].

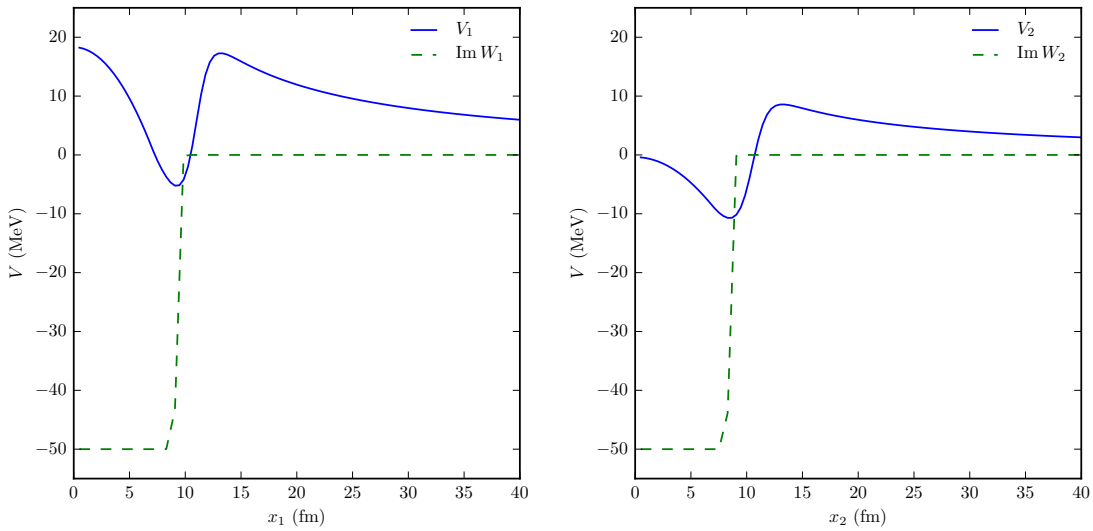

Figure 2.4.1: Total interaction potential V (solid line) and imaginary part of the fusion potential W (dashed line) for the ^{209}Bi–^{4}He subsystem (left panel) and for the ^{209}Bi–^{2}H subsystem (right panel).

Table 2.4.1: Parameters of the Woods-Saxon imaginary absorbing potential used for the different binary systems in the present calculations.

system	W_{0i} (MeV)	x_{0i} (fm)	a_{0i} (fm)
^{209}Bi–^{4}He	-50.0	9.24	0.1
^{209}Bi–^{2}H	-50.0	8.48	0.1

W_{T1} and W_{T2} are constructed in terms of the x_1 and x_2 coordinates which are the distances between target and fragment 1 or 2. The relationship between the total absorbing potential $W(R, \xi, \theta)$ expressed as a function of the coordinates x_1, x_2 and in terms of R, ξ θ is:

$$\hat{W}_{T1}(x_1) + \hat{W}_{T2}(x_2) = \hat{W}(R, \xi, \theta). \tag{2.26}$$

From Eq. (2.24) and Eq. (2.26) it follows that:

$$\hat{\gamma} = \tanh^{-1} \frac{\sinh \hat{\gamma}_1 + \sinh \hat{\gamma}_2}{\cosh \hat{\gamma}_1 + \cosh \hat{\gamma}_2 - 1}, \tag{2.27}$$

where the operators $\hat{\gamma}_1(x_1)$ and $\hat{\gamma}_2(x_2)$ are determined from Eq. (2.24). The individual imaginary potentials are constructed replacing x_1 and x_2 by their expressions in terms of

R, ξ and θ coordinates:

$$x_1 = \sqrt{R^2 + a^2\xi^2 - 2R\xi a\cos\theta}, \tag{2.28}$$

$$x_2 = \sqrt{R^2 + b^2\xi^2 + 2R\xi b\cos\theta}, \tag{2.29}$$

where the factors a and b are constants related to the mass, $a = M_2/M_{\rm TOT}$ and $b = M_1/M_{\rm TOT}$ with $M_{\rm TOT} = M_1 + M_2$. The quantity $e^{-\hat{\gamma}}$ acts as a damping factor for the wave function and thus the recursive relation for the Chebychev polynomials is redefined as:

$$\mathrm{e}^{-\hat{\gamma}} Q_{n-1}(\hat{H}_{\rm norm}) + \mathrm{e}^{\hat{\gamma}} Q_{n+1}(\hat{H}_{\rm norm}) - 2\hat{H}_{\rm norm} Q_n(\hat{H}_{\rm norm}) = 0 \tag{2.30}$$

with the initial condition: $Q_1(\hat{H}_{\rm norm}) = \mathrm{e}^{-\hat{\gamma}}\hat{H}_{\rm norm}$. In the case of no absorption the factor $\mathrm{e}^{-\hat{\gamma}} = 1$ and the wave function preserves its norm. On the other side, when the absorption is present the quantity $\mathrm{e}^{-\hat{\gamma}}$ becomes smaller (tends to zero), the wave function is damped and its norm is no longer preserved. In this work, $\Delta t = 10^{-22}$ s, and in absence of the imaginary potentials the norm of the wave function is preserved with an accuracy of $\sim 10^{-14}$.

2.5 Fusion cross sections

In this work I focus on the total, incomplete and complete fusion cross sections: $\sigma_{\rm TF}$, $\sigma_{\rm ICF}$ and $\sigma_{\rm CF}$. A limitation of most fusion models involving weakly bound nuclei is the lack of an unambiguous way to disentangle $\sigma_{\rm CF}$ and $\sigma_{\rm ICF}$. The key idea to overcome this issue is to examine the location of each fragment with respect to the position of the individual Coulomb barriers, irrespective of the internal excitation of the ^{6}Li projectile: if a fragment is located inside the Coulomb barrier it is captured by the target. A CF event is identified when both fragments are located inside their individual barriers, while an ICF event occurs when just one of the fragments is inside its barrier. This idea is realised by means of position projection operators:

$$\hat{P}_j = \Theta(R_B^{jT} - x_j) \tag{2.31}$$

$$\hat{Q}_j = \hat{1} - \hat{P}_j \tag{2.32}$$

where $\Theta(x)$ is the Heaviside step function and R_B^{jT} are the locations of the Coulomb barriers in the fragment j – target interaction. The projection operators satisfy the properties: $\hat{P}_j^2 = \hat{P}_j$, $\hat{Q}_j^2 = \hat{Q}_j$, and $\hat{P}_j\hat{Q}_j = 0$. Applying the identity operator, $\hat{I} = (\hat{P}_1 + \hat{Q}_1)(\hat{P}_2 + \hat{Q}_2)$, on the total wave function $\Psi^{JK}(R, \xi, \theta)$, the wave function can be decomposed into three

parts:

$$\Psi^{JK}_{\mathrm{CF}}(R,\xi,\theta) = \hat{P}_1\hat{P}_2\Psi^{JK}(R,\xi,\theta), \tag{2.33}$$

$$\Psi^{JK}_{\mathrm{ICF}}(R,\xi,\theta) = (\hat{P}_1\hat{Q}_2 + \hat{Q}_1\hat{P}_2)\Psi^{JK}(R,\xi,\theta), \tag{2.34}$$

$$\Psi^{JK}_{\mathrm{SCATT}}(R,\xi,\theta) = \hat{Q}_1\hat{Q}_2\Psi^{JK}(R,\xi,\theta). \tag{2.35}$$

Each of these parts is associated with a specific physical processes described in figure 2.0.1. The *scattering* wave function $\Psi^{JK}_{\mathrm{SCATT}}$ corresponds to events where both the fragments are located outside of their Coulomb barriers and thus are not captured by the target (NCBU event). The decomposition of the wave function is implemented by calculating the values of x_1 and x_2 for each combination of (ξ, R, θ) and comparing them with the associated Coulomb barrier locations.

Figure 2.5.1 shows the domains where the different contributions of the total wave function are defined for one value of the angle θ. The domain for events associated with complete fusion is marked in red. Such events require both of the projectile fragments to be fused with the target which means that x_1 and x_2 should be small (smaller than the barrier locations which are both smaller than 10 fm). From the definition of x_1 and x_2 in terms of (ξ, R, θ) the figure can be understood as follows: if the projectile or its constituents separately tunnelled through the barrier, the center of mass of the projectile is close to the target. This implies that the values of the coordinate R which correspond to the CF domain cannot be large. The distance between the constituents has more freedom to vary: if it's small, it could be understood that the projectile as a whole was fused. While if it's large, the projectile dissociated and the individual fragments were captured. The dark and light blue areas represent the domains of the incomplete fusion 1 and 2. The first one describes the situation where ^{4}He is captured while ^{2}H escaped. The second one is the opposite situation. The projectile dissociated, this means that the domains are shifted to larger values of ξ. The values of R can be larger than those associated with the CF domain because the center of mass of the projectile does not coincide with one fragment and since one of the fragment escaped and is relatively far from the target. The green area represent the domain connected to the so called scattering event, where none of the fragments is captured. The sum of the four regions completely overlaps with the domain associated to the total wave function.

The TF cross section, σ_{TF}, is derived from the continuity equation for the probability current of the total wave function:

$$\sigma_{\mathrm{TF}} = \frac{2}{\hbar\, v}\langle\Psi|W_{T1}(x_1) + W_{T2}(x_2)|\Psi\rangle, \tag{2.36}$$

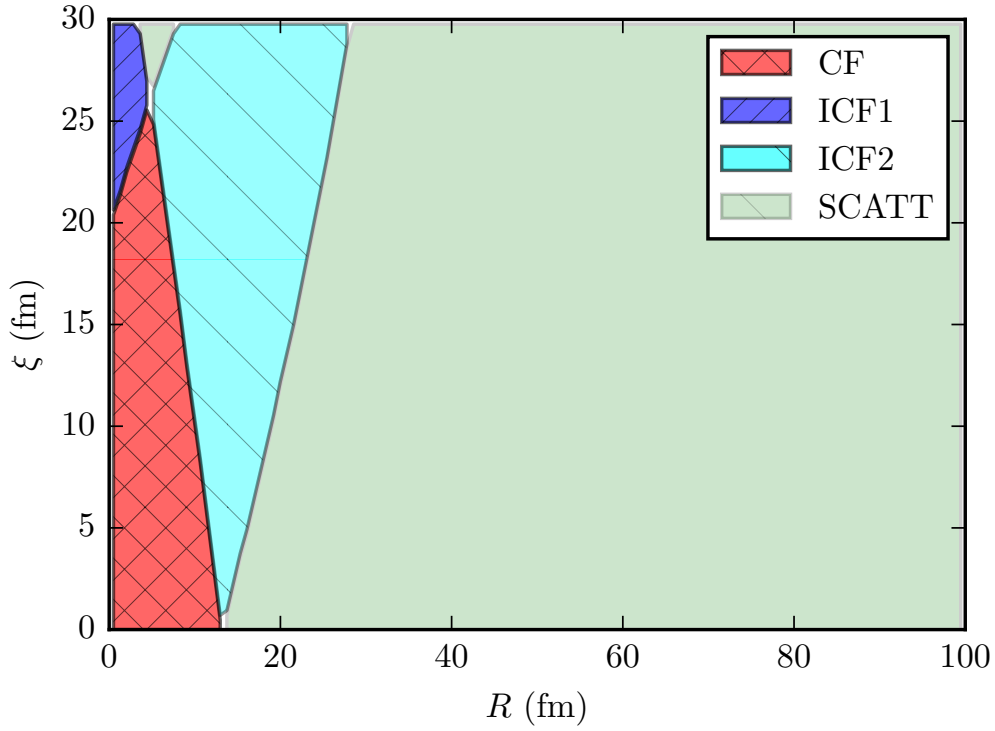

Figure 2.5.1: Domains of the different components of the wave function corresponding to incomplete fusion $\Psi_{\rm ICF}$ (ICF1 and ICF2), complete fusion $\Psi_{\rm CF}$ and scattering $\Psi_{\rm SCATT}$.

where $v = \hbar K_0/(\mu_{TP}V)$ with V a unit volume of the target. By making use of the wave function decomposition, the CF and ICF cross sections can be expressed as:

$$\sigma_{\rm CF} = \frac{2}{\hbar v}\langle\Psi_{\rm CF}|W_{T1}(x_1) + W_{T2}(x_2)|\Psi_{\rm CF}\rangle, \tag{2.37}$$

$$\sigma_{\rm ICF} = \frac{2}{\hbar v}\langle\Psi_{\rm ICF}|W_{T1}(x_1) + W_{T2}(x_2)|\Psi_{\rm ICF}\rangle. \tag{2.38}$$

The CF cross section in Eq. (2.37) also includes contributions from the *sequential fusion*, when the projectile breakup is followed by fusion of all the projectile constituents with the target.

2.6 Energy-resolved fusion cross sections

The fusion cross sections are calculated after a "long" period of time, using $\Psi(t = t_f)$, as $\sigma_{\rm CF}$ and $\sigma_{\rm ICF}$, which should be compared to experimental data, must be stationary values of Eq. (2.37) and (2.38). Moreover, these cross sections are obtained using an incident wave

packet of initial average energy E_0. But experimental cross sections are determined for a specific incident energy (within certain accuracy) and not for a bulk of energies as that carried by the wave packet. Therefore, one needs to calculate the *energy-resolved* cross sections, for which the window operator method is used [55].

The energy-resolved fusion cross section are proportional to the transmission coefficient through the Coulomb barrier:

$$\sigma(E) = \frac{\pi\hbar^2}{2\mu_{TP}E}\sum_J (2J+1)\mathcal{T}^J(E) \tag{2.39}$$

where each fusion process (TF, ICF and CF) has its own transmission coefficient $\mathcal{T}^J(E)$.

Having calculated the transmission coefficient for TF and CF using the window operator method, the transmission coefficient for ICF can be determined by $\mathcal{T}_{ICF}(E) = \mathcal{T}_{TF}(E) - \mathcal{T}_{CF}(E)$.

The window operator method The key idea of the window operator method is to calculate the energy spectrum, $\mathcal{P}(E_k)$, of the initial and final wave functions. E_k is the centroid of a total energy bin of width 2ϵ. A vector of reflection coefficients, $\mathcal{R}(E_k)$, is determined by the ratio:

$$\mathcal{R}(E_k) = \frac{\mathcal{P}^{final}(E_k)}{\mathcal{P}^{initial}(E_k)} \tag{2.40}$$

The transmission coefficients are then:

$$\mathcal{T}(E_k) = 1 - \mathcal{R}(E_k) \tag{2.41}$$

The energy spectrum is calculated as $\mathcal{P}(E_k) = \langle\Psi|\hat{\Delta}|\Psi\rangle$, where $\hat{\Delta}$ is the window operator:

$$\hat{\Delta}(E_k, n, \epsilon) \equiv \frac{\epsilon^{2^n}}{(\hat{\mathcal{H}}_{\text{asy}} - E_k)^{2^n} + \epsilon^{2^n}} \tag{2.42}$$

$\hat{\mathcal{H}}_{\text{asy}}$ is the asymptotic part of the Hamiltonian where the nuclear contribution to the potential V is neglected and n determines the shape of the window function. As n is increased, this shape rapidly becomes rectangular with very little overlap between adjacent energy bins, the bin width remaining constant at 2ϵ. The spectrum is constructed for a set of E_k where E_{k+1}=E_k+2ϵ. In this work, n= 2 and $\epsilon = 0.25$ MeV. Solving two successive linear equations for the vector $|\chi\rangle$:

$$(\hat{\mathcal{H}}_{\text{asy}} - E_k + \sqrt{\text{i}}\epsilon)(\hat{\mathcal{H}}_{\text{asy}} - E_k - \sqrt{\text{i}}\epsilon)|\chi\rangle = |\Psi\rangle \tag{2.43}$$

yields $\mathcal{P}(E_k) = \epsilon^4 \langle \chi | \chi \rangle$. Figure 2.6.1 shows the spectrum in energy of the wave function of the system obtained employing the window operator method with a width $\epsilon = 0.25$MeV. The comparison with the energy distribution of the initial wave packet $\Phi_0(R)$ illustrates how the method works. Note that, when applied to the Ψ_{CF}, the asymptotic Hamiltonian is replaced by the full Hamiltonian since the complete fusion wave function is localised in a region where the nuclear part of the interaction is not negligible.

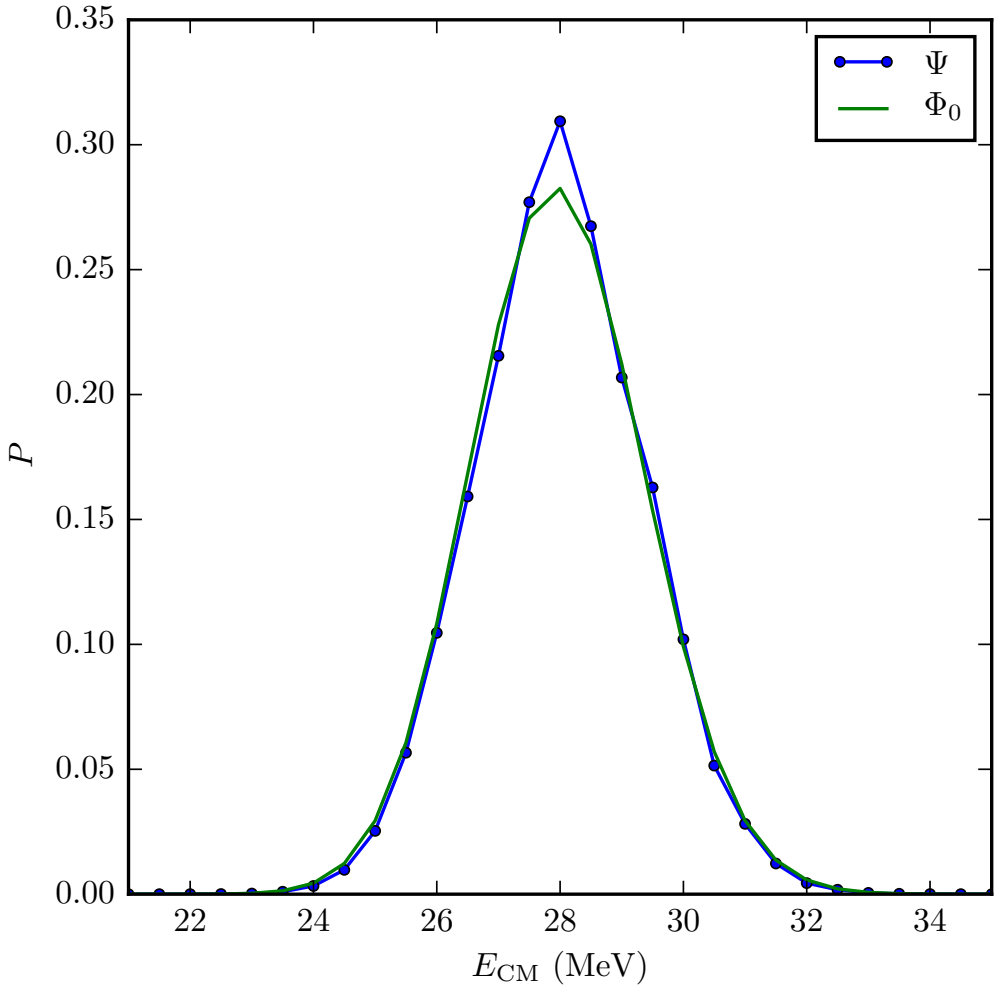

Figure 2.6.1: Spectrum in energy of the total wave function calculated with the window operator method (cirlces) and the spectrum of the initial Gaussian wave packet (solid line).

Chapter 3

Results

3.1 One-dimensional results

3.1.1 Test of the propagation

As for the three-dimensional version, the time dependent Schrödinger equation is solved expanding the evolution operator in a series of Chebychev polynomials. The same imaginary potentials W_1 and W_2 that simulate the irreversibility of fusion by acting on the wave function as damping factors are used. Figure 3.1.1 shows the evolution in time of $\|\Psi(R,\xi)\|^2$ and of the expectation value of the Hamiltonian of the system. The result is similar to the one obtained with the three-dimensional calculation. A drop in both quantities occurs around $t \approx 40 \times 10^{-22}$ s continues until $t \approx 50 \times 10^{-22}$ s. For later times, the two quantities remain constant indicating that the stationary regime is reached.

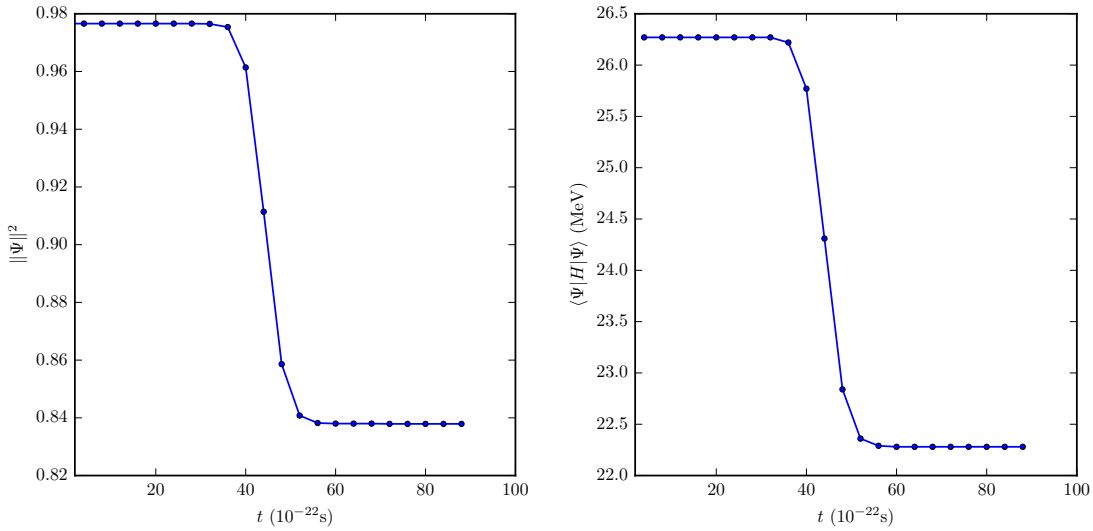

Figure 3.1.1: The norm of the wave function squared $\|\Psi\|^2$ (left panel) and the expectation value of $\hat{H}$ (right panel) as function of time.

3.1.2 Fusion cross sections

The transmission coefficients through the barrier were analysed for each fusion process individually by running the calculation with different values of the initial average energy of the Gaussian wave packet E_0 and the result are shown in figure 3.1.2. The triangles refer to the run with $E_0 = 33$ MeV, the circles to $E_0 = 28$ MeV, the squares to $E_0 = 25$ MeV and the crosses to $E_0 = 23$ MeV. For total and incomplete fusion, the curves show an overlap which is better at high energies. At low energies, the overlap appears to be just in one point among the runs with $E_0 = 23$ MeV and $E_0 = 25$ MeV.

The cross sections associated with incomplete and complete fusion converged transmission coefficients have been calculated and compared with experimental data of [56]. Figure 3.1.3 shows the result of the comparison. In none of the cases an agreement was reached, as it was expected being the theoretical results only at the one-dimensional level. For the incomplete fusion cross section the theoretical results seem to show a similar qualitative dependency on the energy. For the complete fusion cross section this seems to be true as well only for the low energy data.

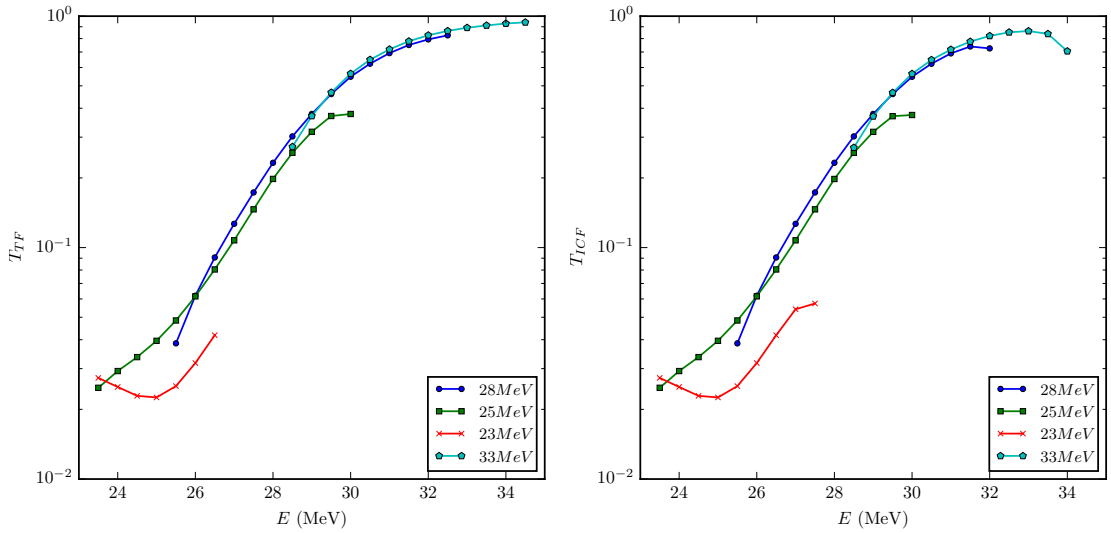

Figure 3.1.2: The first panel on the left shows the transmission coefficients through the Coulomb barrier related to a *total fusion* event. The panel to the right shows the transmission coefficients associated with an *incomplete fusion* event.

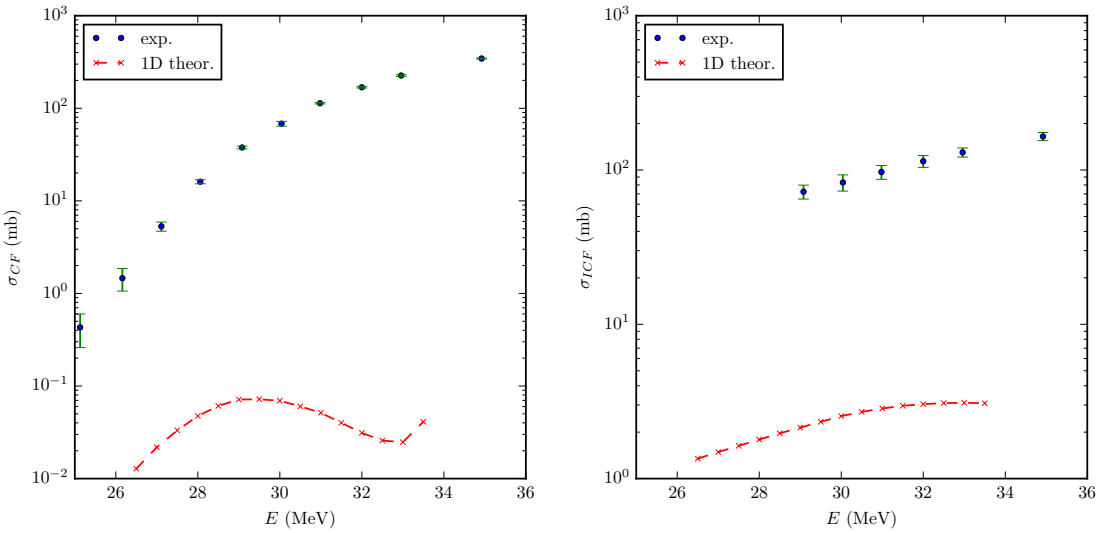

Figure 3.1.3: Experimental complete (left panel) and incomplete (right panel) fusion cross section compared with the one-dimensional results.

3.2 Three-dimensional results

3.2.1 Test of the propagation

Given the wave function of the system at the initial time t_0, solving the time dependent Schrödinger equation by means of the modified Chebychev propagator as explained in 2.4, allows to compute the wave function at any desired time t. In order to calculate the observables a stationary regime has to be reached, where the projectile or part of its constituents that did not fuse with the target are travelling back abandoning the interaction region. Figure 3.2.1 shows the evolution in time of $\|\Psi\|^2$ and $\langle\Psi|\hat{H}|\Psi\rangle$. From this figure it is possible to have an insight of what is happening at the system once the projectile starts approaching the target. For instance, both the quantities remain constant until time $t \approx 40 \times 10^{-22}$ s. In this moment, the projectile approaches the interaction region and starts "feeling" the repulsive Coulomb part of the potential. A certain amount of incident flux will be reflected from the Coulomb barrier, while the remaining flux will be transmitted tunnelling through the barrier. This is the reason of the drop in $\|\Psi\|^2$ and in the expectation value of $\hat{H}$, because part of the incident flux was transmitted and then absorbed by the target. Starting from $t \approx 60 \times 10^{-22}$ s, there is no more loss of flux and this can be seen from $\|\Psi\|^2$ and $\langle\Psi|\hat{H}|\Psi\rangle$ that do not change anymore with time. To stop the time propagation which calculates the wave function at a time t, two conditions have

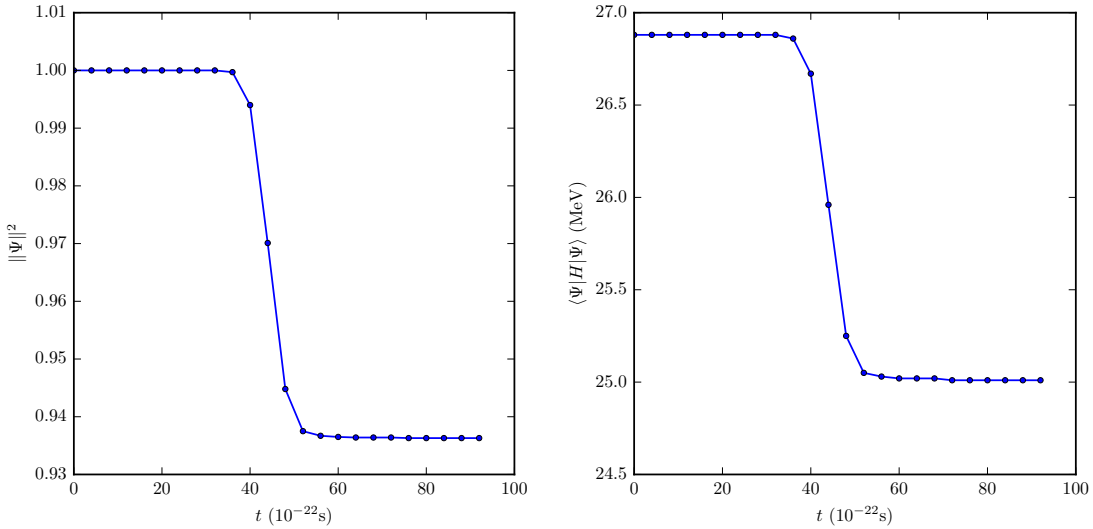

Figure 3.2.1: The norm of the wave function squared $\|\Psi\|^2$ (left panel) and the expectation value of $\hat{H}$ (right panel) as function of time.

to be fulfilled sequentially. First, the mean value of the coordinate R is calculated and then, if it is larger than R_0, the k_R-momentum distribution is analysed. If the distribution is peaked around positive values of momenta, the reflected flux is moving backwards (from left to right). The stationary regime is thus reached.

Figure 3.2.2 shows the evolution in time of the one-dimensional density of the wave function with respect to the R coordinate. At time t_0 the density is a Gaussian distribution centered around $R_0 = 120$ fm. Then, for $t \approx 40 \times 10^{-22}$ s the Gaussian shape is distorted, indicating that the effect of the repulsive Coulomb barrier became important and that every energy component which forms the wave packet is affected by this in a different way. At $t \approx 70 \times 10^{-22}$ s, the wave packet is travelling back, but comparing the height of the peak with that at initial time, it is clear that a certain amount of the initial flux tunnelled through the barrier and was absorbed by the target. For later times, the wave packet keeps travelling towards right. The height of the peak decreases further indicating that at the previous time some energy components still did not reach the interaction region and were still not affected by the repulsive barrier. The spreading in width is due to the scattering of the different energy components of the wave packet.

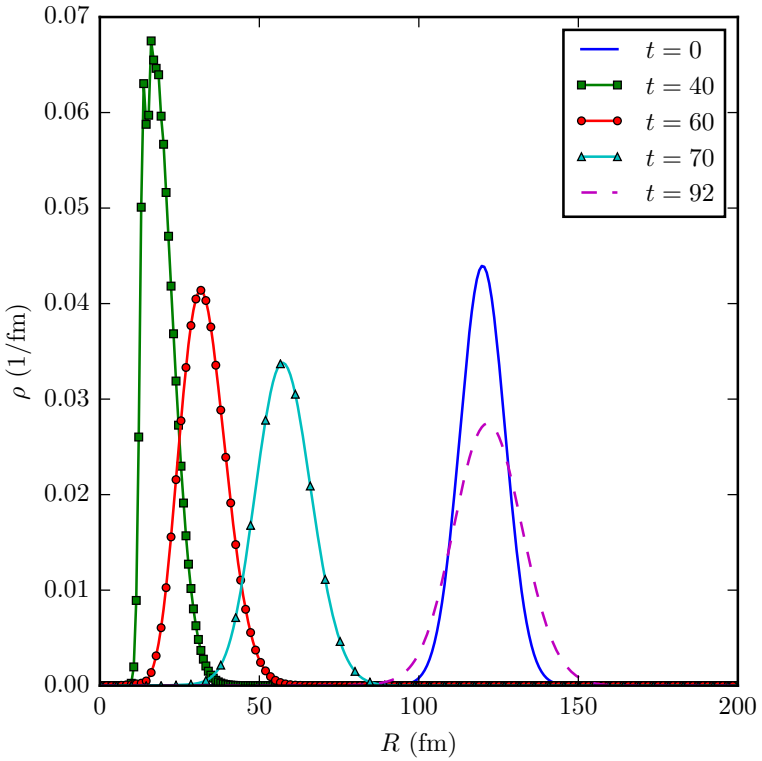

Figure 3.2.2: The evolution in time of the density of probability of the projectile-target relative motion wave function. The solid line shows the initial location of the wave packet along the grid. The dotted-dashed curve represents the moment when the wave packet reaches the Coulomb barrier. The circles, crosses and squares describe the motion of the part of the wave packet.

3.2.2 Fusion cross sections

Using the wave function calculated at time $t = t_f$, where t_f refers to the time when the stationary regime is reached, I calculated the transmission coefficients through the Coulomb barrier. By making use of Eq. (2.33) and (2.35), the transmission coefficient $T(E)$ associated with one particular fusion process is computed. In this way it is possible to disentangle the contributions of the complete and incomplete fusion processes. I calculated the transmission coefficients associated with each fusion process separately for different values of the initial average incident energy of the Gaussian wave packet. The result is shown in Fig. 3.2.3. The triangles refer to an average energy $E_0 = 33$ MeV, the circles to $E_0 = 28$ MeV, the squares to $E_0 = 25$ MeV and the crosses to $E_0 = 23$ MeV. The window operator method, which allows to extract the energy dependence of the wave function, is

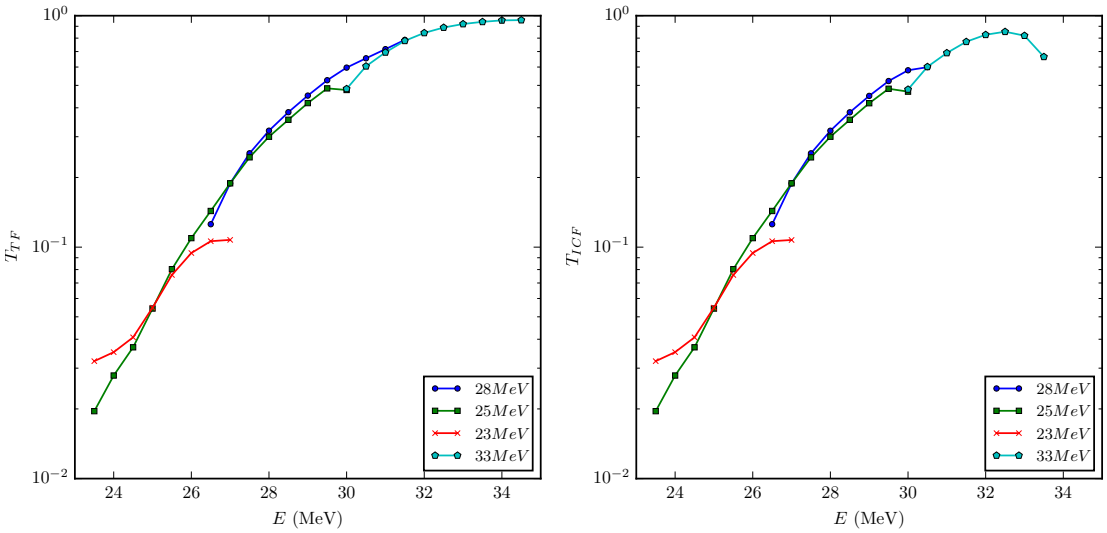

Figure 3.2.3: Transmission coefficients through the Coulomb barrier. The first panel on the left shows the results associated with a *total fusion* event. The panel to the right refers to an *incomplete fusion* event.

reliable for a range of energies around the initial average energy of the incident wave packet E_0. This means that the whole curve cannot be obtained from a single calculation run at a given E_0. But the overlap among the curves indicates that few runs with different E_0 are enough to reconstruct the full curve over a broad range of energies. Figure 3.2.3 shows the transmission coefficients as a function of the incident energy related to the three fusion events separately for $J = 0$ and $K = 0$. On the first row to the left it is shown the result associated with the total fusion. On the right, that for incomplete fusion. And on the second row it is displayed the result for complete fusion.

3.2.3 Sensitivity of $T(E)$ to the model parameters

To test the sensitivity of the results to the parameters of the model, I performed some calculations where I varied one parameter at a time, keeping the others fixed. I chose to look at the effect of a change in a given parameter on the total fusion transmission coefficient. In figure 3.2.4 the *converged* transmission coefficients for total fusion are shown where the parameters under investigation are the spatial width of the Gaussian wave packet σ, its initial location along the grid R_0 and the width parameter in the window operator method ϵ. By *converged* curve it is meant the curve that covers the whole energy range and that was constructed using the results of few calculations run at different initial average

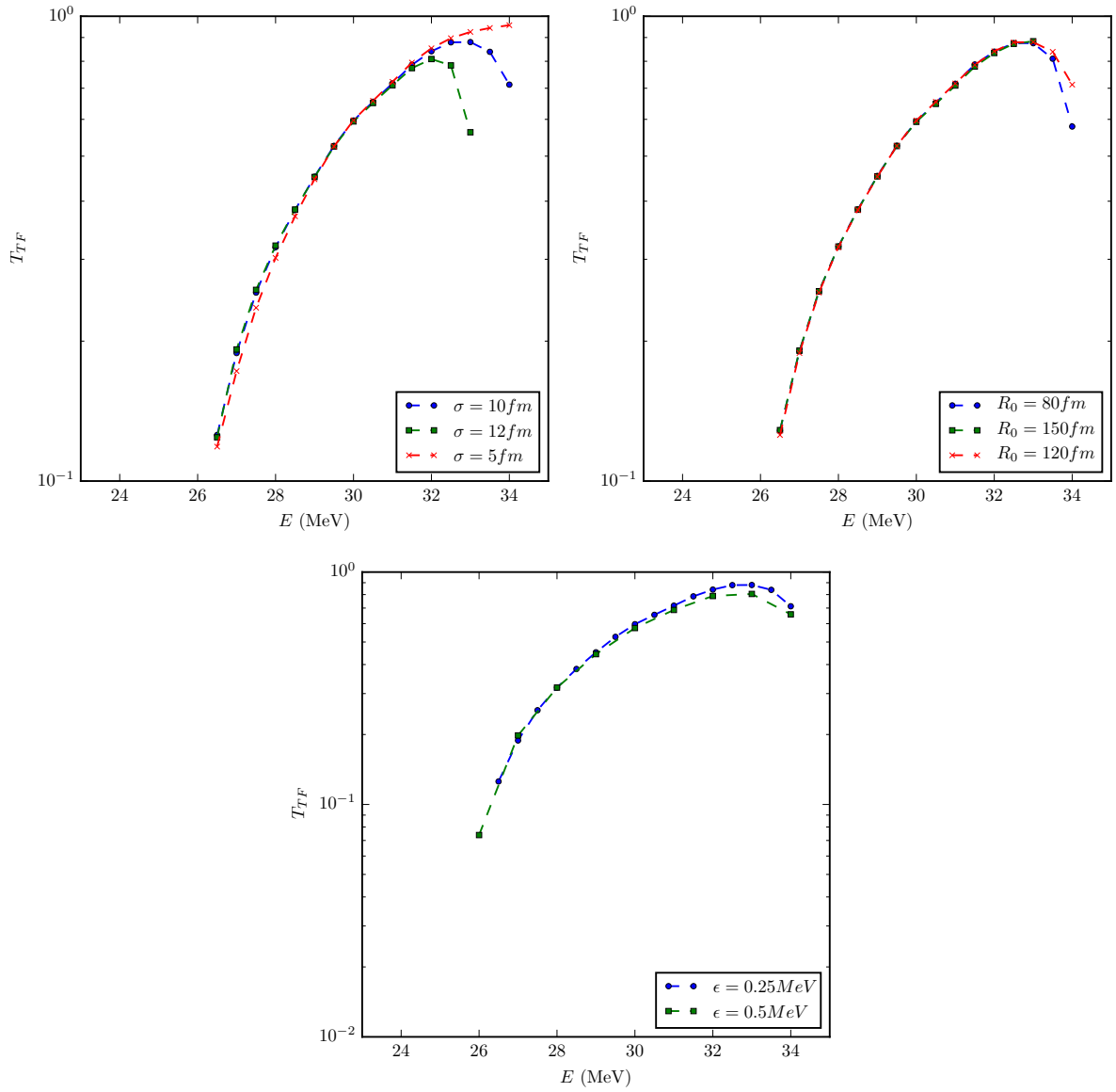

Figure 3.2.4: Transmission coefficients related to a *total fusion* process. On the left in the first row, for different values of σ. On the right, for different values of $R0$. On the second row for different ϵ.

energy E_0. Three values of $\sigma = 5, 10, 12$ fm, three for $R_0 = 80, 120, 150$ fm and two for $\epsilon = 0.25, 0.5$ MeV have been tested. In all the cases the resulting curves agree very well, indicating that the calculation does not depend sensitively on these parameters of the model.

3.2.4 Comparison with experimental data

From the total fusion transmission coefficients, the cross section associated with this process has been calculated through Eq. (2.39) and compared with experimental data of [56]. Results are shown is Figure 3.2.5. The crosses refer to the result obtained from the one-dimensional model, the squares show the three-dimensional results while the circles are the experimental data. The theoretical results obtained from the three-dimensional model agree qualitatively with the data but still overestimate them over the whole energy range. The reason for this lies in the fact that the transmission coefficients for each value of J were extrapolated from those at $J = 0$ by means of the *energy-shifting formula* [57]. This is not the same as performing the "exact" calculation for each value of J. The results obtained from the one-dimensional model are shown to illustrate that in order to obtain some insight in the physical process, the one-dimensional approximation is definitely not enough.

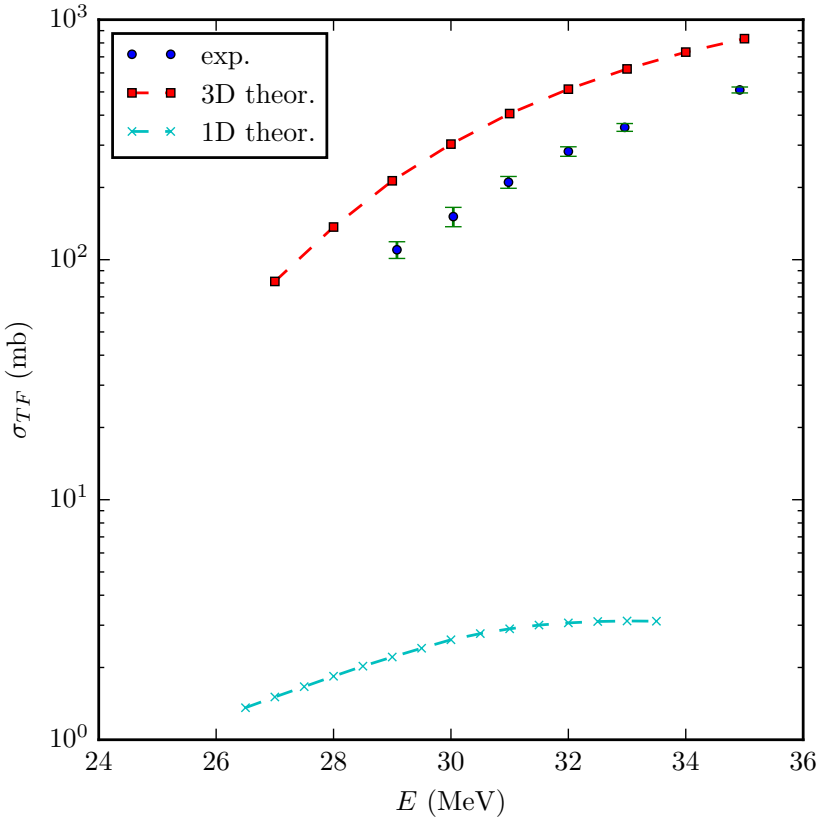

Figure 3.2.5: Comparison of theoretical and experimental total fusion cross section.

3.2.5 Comparison with the energy-shifting formula

The transmission coefficients for total fusion are calculated for two different values of total angular momentum J and compared to the approximations obtained by means of the energy-shifting method. Figure 3.2.6 shows that for $J = 10$ the two methods provide essentially the same result. While for $J = 20$ the curves start to diverge, especially at low energies. The effect of the Coriolis coupling was checked by comparing the results for the total fusion transmission coefficients at $J = 0, K = 0$ (circles) with those at $J = 4, K = 4$ (crosses). The effect is found to be very weak. The comparison is shown in Fig. 3.2.7.

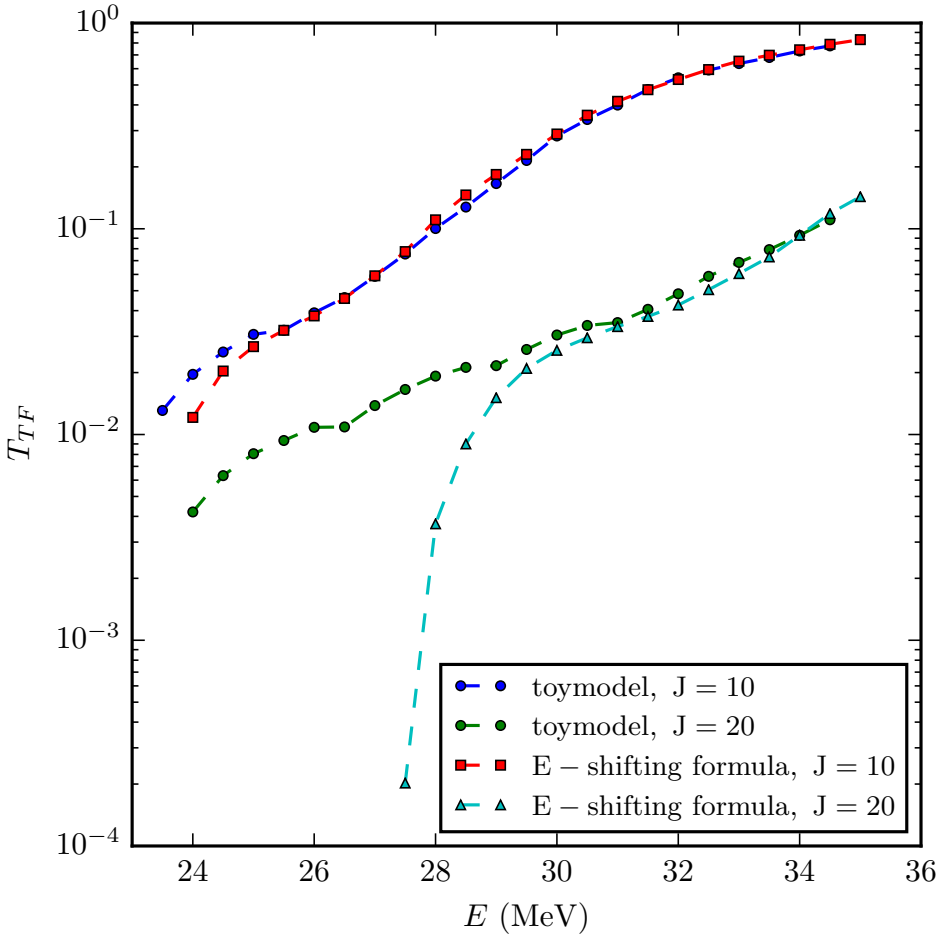

Figure 3.2.6: Transmission coefficients compared to the results of the energy-shifting formula.

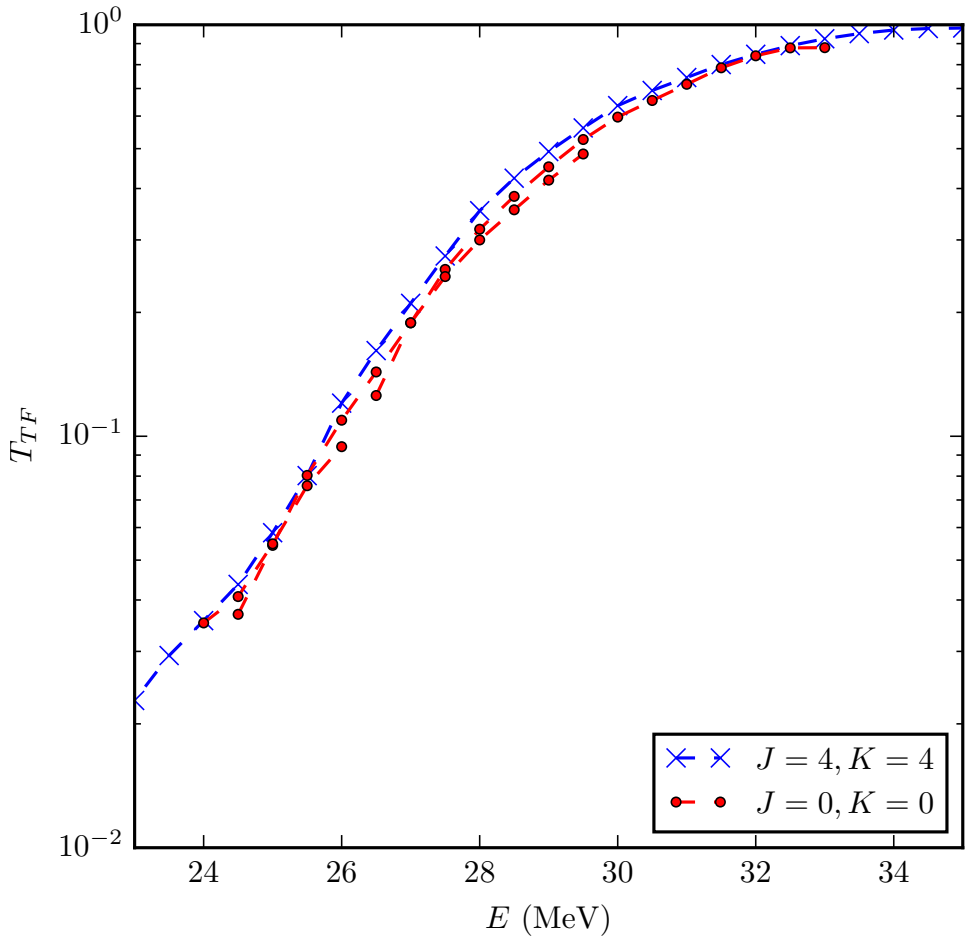

Figure 3.2.7: Converged curves for the transmission coefficients obtained from a calculation with $K = 0$ and $K = 4$.

3.2.6 Comparison between one and three dimensional models

I compared the results I obtained from the one-dimensional model and those from the three dimensional one for the converged total fusion transmission coefficients. Figure 3.2.8 shows the comparison. The transmission coefficients of the three-dimensional version of the model are higher in magnitude over all the energy range considered apart from the last values at high energy.

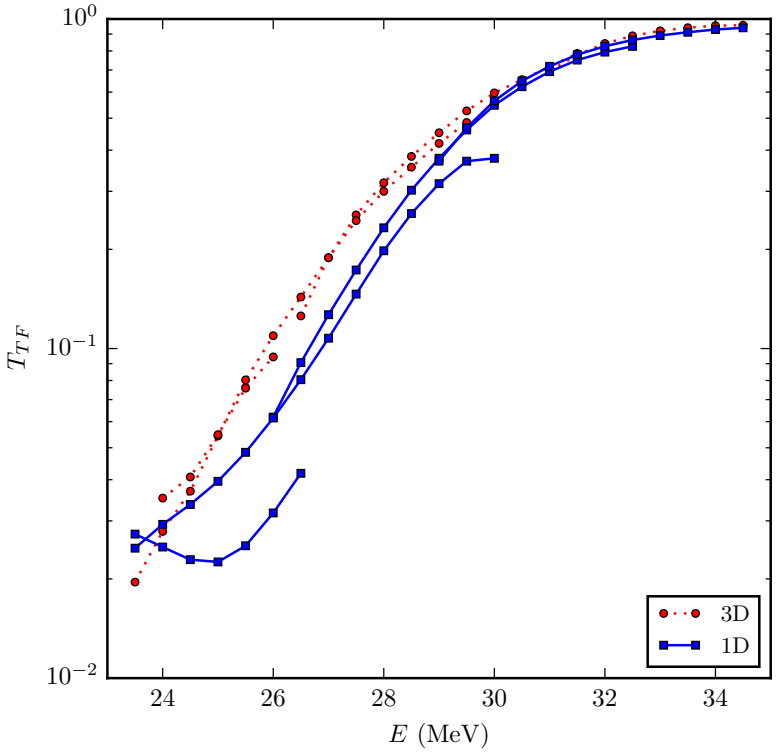

Figure 3.2.8: Converged transmission coefficients obtained from the one-dimensional model (squares) and the three-dimensional version (circles).

Chapter 4

Conclusions and outlook

In the present work, I developed a theoretical model for the study of collisions of weakly bound nuclei on stable targets. Among the different processes that can occur during this type of collisions I focused on fusion reactions. In particular, the model was designed to distinguish contributions of *incomplete* and *complete* fusion processes. The peculiarity of the collisions involving a weakly-bound projectile is due to its ease of dissociating, leading to the fact that, at a given incident energy, several reaction channels are open simultaneously. The work was focused on the development of a quantum theoretical model which would be able to describe quantitatively various processes at the same time. This would allow to study the link between the internal structure (reflected in the break up probability) of a weakly-bound projectile such as a halo nucleus, and the probability for the different fusion processes. First I implemented the relevant one-dimensional computer code and used $^{6}\mathrm{Li} - {}^{209}\mathrm{Bi}$ system to test the model. Subsequently I extended the model to perform calculations in three dimensions in order to compare the results of calculations with experimental data. One of the main motivations for such studies is the important role of halo nuclei in different astrophysical processes. At the same time, obtaining information about the internal structure and reaction mechanisms of halo nuclei is also relevant from the experimental point of view due to many planned experiments with radioactive ion beams at research facilities.

The model developed in this work is based on solving the time-dependent Schrödinger equation within the Chebychev propagator scheme. The advantage of time-dependent method is that a single propagation of the wavepacket provides results for a wide range of energies. The total wave function was decomposed into three parts associated with *scattering*, *incomplete* and *complete* fusion processes by projector operators defined in coordinate space. A damping factor for each projectile constituent was introduced which simulates the irreversibility of the fusion process, by removing flux from the entrance channel. Using the relevant part of the total wave function I calculated simultaneously the transmission coefficients through the Coulomb barrier associated with the total, incomplete and complete fusion processes and obtained converged curves in both models.

Sensitivity of the results was tested with respect to the parameters of the model. It was shown that there is very weak dependence of the results on the model parameters.

I compared my results for the transmission coefficients associated with total fusion for the total angular momentum $J = 10, 20$ with a calculation based on the energy shifting formula and found a good agreement between the models only for the $J = 10$ case, indicating the limit of the energy-shifting formula approximation.

The one-dimensional converged curves for total fusion transmission coefficients were compared against their three-dimensional versions. The comparison of the one-dimensional complete and incomplete fusion cross section with experimental data indicates that the effect is significant.

I compared my results for the total fusion cross section (using the transmission coefficients at $J = 0$ and successively extrapolated to higher J-values by means of the energy-shifting formula) with experimental data. The agreement is only at a qualitative level indicating once again that the extrapolation method is an approximation.

At the moment, the calculations are computationally demanding and we plan to perform more complete calculations on larger computers in order to be able to compare the present model with experimental data at the quantitative level. Moreover, the model can be used to extract other relevant observables such as the direct reaction cross sections of transfer and breakup processes.

References

[1] M. Cubero et al., Phys. Rev. Lett. 109:262701 (2012)

[2] J.P. Fernández-García et al., Phys. Rev. Lett. 110:142701 (2013)

[3] A. Navin et al., Phys. Rev. C 70:044601 (2004)

[4] A. Lemasson et al., Phys. Rev. Lett. 103:232701 (2009)

[5] A. Di Pietro et al., Phys. Rev. Lett. 105:022701 (2010)

[6] http://www.frib.msu.edu/content/scientific-opportunities

[7] http://www.fair-center.eu/public/experiment-program.html

[8] http://www.riken.jp/en/research/labs/rnc

[9] M. Wiescher, F. Käppeler and K. Langanke, Annual Rev. of Astronomy and Astrophysics 50:165-210 (2012)

[10] I. Tanihata et al. Phys. Lett. B 160:380 (1985)

[11] P.G. Hansen and B. Jonson, Europhys. Lett. B 160:409 (1987)

[12] S.C. Pieper and R.B. Wiringa, Annu. Rev. Nucl, Part. Sci. 51:53 (2001)

[13] P. Navrátil, J.P. Vary, and B.R. Barrett, Phys. Rev. C 62: 054311 (2000)

[14] Sofia Quaglioni and Petr Navrátil, Phys. Rev. Lett. 101: 092501 (2008)

[15] S. Baroni, P. Navrátil, S. Quaglioni, arXiv:1301.3450

[16] G. Hagen, D.J. Dean, M. Hjorth-Jensen and T. Papenbrock, Phys. Lett. B 656:169-173 (2007)

[17] D.B. Kaplan, M.J. Savage, and M.B. Wise, Nucl.Phys.B 534:329 (1998)

[18] U. van Kolck, Nucl.Phys. A 645:273 (1999)

[19] R.J. Glauber, in Lectures in Theoretical Physics, ed. W.E. Brittin (Interscience, N.Y., 1959) Vol. 1, 315.

[20] P. Capel, D. Baye and V.S. Melezhik, Phys. Rev. C 68:014612 (2003)

[21] K. Ogata, M. Yahiro, Y. Iseri, T. Matsumoto and M. Kamimura, Phys. Rev. C 68:064609 (2003)

[22] D. Baye, P. Capel and G. Goldstein, Phys. Rev. Lett. 95:082592 (2005)

[23] G. Goldstein, D. Baye and P. Capel, Phys. Rev. C 73:024602 (2006)

[24] M. Kamimura et al., Prog. Theor. Phys. Supp. 89:1 (1986)

[25] B.B. Back, H. Esbensen, C.L. Jiang and K.E. Rehm, Rev. Mod. Phys. 86:317-360 (2014)

[26] http://www.fair-center.eu/for-users/experiments/nustar.html

[27] http://www.eurisol.org/

[28] A. Diaz-Torres, J. Phys. G.: Nucl. Part. Phys. 37:075109-1-10 (2010)

[29] C. Forssén, P. Navrátil, W.E. Ormand and E. Caurier, Phys. Rev. C 71:044312 (2005)

[30] P. Navrátil, R. Roth and S. Quaglioni, Phys. Lett. B 704:379–383 (2011)

[31] S.C. Pieper, V.R. Pandharipande, R.B. Wiring and J. Calson, nucl-th/0102004

[32] S. Bacca, A. Schwenk, G. Hagen, and T. Papenbrock, Eur.Phys.J. A 42:553 (2009)

[33] S. Bacca, N. Barnea, and A. Schwenk, Phys.Rev. C 86:034321 (2012)

[34] H.W. Hammer and D.R. Phillips, Nucl. Phys.A 865:17 (2011)

[35] X. Zhang, K.M. Nollett, and D.R. Phillips, Phys.Rev.C 89:051602 (2014)

[36] Y. Ogawa, K. Yabana, Y. Suzuki, Nucl. Phys. A 543:722 (1992)

[37] B. Abu-Ibrahim and Y. Suzuki, Phys. Rev. C 61:051601 (2000)

[38] K. Varga, S.C. Pieper, Y. Suzuki and R.B. Wiringa, Phys. Rev. C 66:034611 (2002)

[39] M. Fallot, J.A. Scarpaci, D. Lacroix, P. Chomaz and J. Margueron, Nucl. Phys. A 700:70 (2002)

[40] T. Kido, K. Yabana, and Y. Suzuki, Phys. Rev. C:50, R1276 (1994)

[41] V.S. Melezhik, and D. Baye, Phys. Rev. C 59:3232 (1999)

[42] T. Kido, K. Yabana and Y. Suzuki, Phys. Rev. C 53:2296 (1996)

[43] T. Matsumoto, T. Kamizato, K. Ogata, Y. Iseri, E. Hiyama, M. Kamimura and M. Yahiro, Phys. Rev. C 68:064607 (2003)

[44] K. Ogata, C.A. Bertulani, Prog. Theor. Phys. 121:1399 (2009)

[45] T. Fukui, K. Ogata and P. Capel, Phys. Rev. C 90: 034617 (2014)

[46] A.Diaz-Torres and I.J. Thompson, Phys. Rev. C 65:024606 (2002)

[47] Y. Sun, R.S. Judson and D.J. Kouri, J.Chem. Phys. 90:241 (1989)

[48] B. Poirier, Chem. Phys. 308:305-315 (2005)

[49] J. Tennyson and B. Sutcliffe, J. Chem. Phys. 77:4061 (1982)

[50] P. McGuire and D.J. Kouri, J. Chem. Phys. 60:2488 (1974)

[51] L.C. Chamon et al., Phys. Rev. C 66:014610 (2002)

[52] B.T. Sutcliffe, *The Dynamics of Molecules*, edited by R.G. Wooley, NATO ASI Ser. (Plenum, New York,1980); B.T. Sutcliffe, *Proceedings of XII International Congress of Latin-speaking Theoretical Chemist*, edited by X. Carbo (North-Holland, Amsterdam, 1982)

[53] V.A. Mandelshtam and H.S. Taylor, J. Chem. Phys. 103:2903 (1995)

[54] A. Diaz-Torres, I.J. Thompson and C. Beck, Phys. Rev. C 68:044607 (2003)

[55] K.J. Schafer and K.C. Kulander, Phys. Rev. A 42:5794 (1990)

[56] M. Dasgupta et al., Phys. Rev. C 70:024606 (2004)

[57] A. Diaz-Torres, G.G. Adamian, V.V. Sargsyan and N.V. Antonenko, Phys. Lett. B 739:348-351 (2014)

[58] U. Manthe, *NIC Series, Vol. 10 Quantum Simulations of Complex Many-body Systems: From Theory to Algorithms*, Lecture notes,In.: J.G.,D.M.,A.M., Jülich (2002)

[59] R.Kosloff, *Dynamics of Molecules and Chemical Reactions*, edited by R. E. Wyatt and J. Z. H. Zhang (Marcel Dekker, New York, 1996)

[60] D. Kosloff, R. Kosloff, J. Comp. Phys. 52:35 (1983)

[61] J.C. Light, I.P. Hamilton and J.V. Lill, J. Chem. Phys. 82:1400 (1985)

[62] D.T. Colbert and W.H. Miller, J. Chem. Phys. 96:3 (1992)

[63] S. Sukiasyan and H.-D. Meyer, J.Phys.Chem.A 105:2604-2611 (2001)

[64] D.G. Kanhere, Physics through computation-II, IAPT Physics Education: 55-60 (2007)

[65] M. Krell and T.E.O. Ericson, J. Comp.Phys. 3:202-207 (1968)

[66] H. Tal-Ezer and R. Kosloff, J. Chem. Phys. 81:3967 (1984)

[67] R.T. PAck, J.Chem.Phys. 60:633 (1974)

Appendix A

Derivation of the effective Hamiltonian

In this appendix the derivation of the effective Hamiltonian $\hat{\mathcal{H}}^J_{\text{eff}}$ (2.9) is presented. The expression for the part of the Hamiltonian $\mathcal{H}_2$ defined by Eq. (2.7) consists of several contributions, all proportional to the total angular momentum J or its components J_i. To obtain the effective Hamiltonian $\hat{\mathcal{H}}^J_{\text{eff}}$, first the action of each of these contributions on the total wave function $\Psi^{JK}(R,\xi,\theta)\mathcal{D}^J_{m0K}$ needs to be evaluated. Subsequently the the results are multiplied by $\mathcal{D}^{J*}_{m0K'}$ and integrated over the Euler angles. During the derivation, the ordinary expressions for the action of the angular momentum operators on their eigenfunction are used:

$$\hat{J}^2\mathcal{D}^J_{m0K} = \hbar^2 J(J+1)\mathcal{D}^J_{m0K} \tag{A.1}$$

$$\hat{J}_z\mathcal{D}^J_{m0K} = \hbar K\mathcal{D}^J_{m0K} \tag{A.2}$$

$$\hat{J}_\pm\mathcal{D}^J_{m0K} = \hbar[J(J+1) - K(K\pm 1)]^{1/2}\mathcal{D}^J_{m0K\pm 1}, \tag{A.3}$$

with $\hat{J}_\pm = \hat{J}_x \pm \mathrm{i}\hat{J}_y$. The first term of Eq. (2.7) acts on the wave function as:

$$\frac{1}{2\mu_{TP}R^2}(J^2 - J_z^2)\Psi^{JK}\mathcal{D}^J_{m0K} = \frac{\Psi^{JK}}{2\mu_{TP}R^2}\left[\hbar^2 J(J+1) - \hbar^2K^2\right]\mathcal{D}^J_{m0K} \tag{A.4}$$

and the contribution from the second term is:

$$\frac{\cot^2\theta}{2\mu_{TP}R^2}J_z^2\Psi^{JK}\mathcal{D}^J_{m0K} = \frac{\cot^2\theta}{2\mu_{TP}R^2}\Psi^{JK}\hbar^2K^2\mathcal{D}^J_{m0K}. \tag{A.5}$$

The action of the third therm of Eq. (2.7) on the wave function results in the following expression:

$$\frac{\csc^2\theta}{2\mu_{12}\xi^2}J_z^2\Psi^{JK}\mathcal{D}^J_{m0K} = \frac{\csc^2\theta}{2\mu_{12}\xi^2}\Psi^{JK}\hbar^2K^2\mathcal{D}^J_{m0K}. \tag{A.6}$$

For the evaluation of the contribution of the fourth term of (2.7) the operator $\hat{J}_x$ has to be rewritten in terms of the operators $\hat{J}_\pm$:

$$\frac{\cot\theta}{2\mu_{TP}R^2}(J_xJ_z + J_zJ_x)\Psi^{JK}\mathcal{D}^J_{m0K} \tag{A.7}$$

$$= \frac{\cot\theta}{2\mu_{TP}R^2}\left[\frac{1}{2}(\hat{J}_+ + \hat{J}_-)\hat{J}_z + \hat{J}_z\frac{1}{2}(\hat{J}_+ + \hat{J}_-)\right]\Psi^{JK}\mathcal{D}^J_{m0K} \tag{A.8}$$

$$= \frac{\cot\theta}{2\mu_{TP}R^2}\frac{\hbar^2}{2}\left[\Psi^{JK+1}C^+(2K+1)\mathcal{D}^J_{m0K+1} + \Psi^{JK-1}C^-(2K-1)\mathcal{D}^J_{m0K-1}\right], \tag{A.9}$$

where $C^\pm = [J(J+1) - K(K\pm1)]^{1/2}$. Finally, the last term of Eq. (2.7) yields:

$$\begin{aligned}\frac{\hbar}{\mathrm{i}\mu_{TP}R^2}\left(\frac{\partial}{\partial\theta}J_y + \frac{\cot\theta}{2}J_y\right)\Psi^{JK}\mathcal{D}^J_{m0K}& \\ = \frac{\hbar^2}{2\mu_{TP}R^2}\left[C^-\mathcal{D}^J_{m0K-1}\left(\frac{\partial}{\partial\theta} + \frac{\cot\theta}{2}\right)\Psi^{JK-1}\right.& \\ \left. - C^+\mathcal{D}^J_{m0K+1}\left(\frac{\partial}{\partial\theta} + \frac{\cot\theta}{2}\right)\Psi^{JK+1}\right].&\end{aligned} \tag{A.10}$$

Combining Eq. (A.7) and (A.10) results in:

$$\begin{aligned}\left[\frac{\cot\theta}{2\mu_{TP}R^2}(J_xJ_z + J_zJ_x) + \frac{\hbar}{\mathrm{i}\mu_{TP}R^2}\left(\frac{\partial}{\partial\theta} + \frac{\cot\theta}{2}\right)J_y\right]\Psi^{JK}\mathcal{D}^J_{m0K}& \\ = \frac{\hbar^2}{2\mu_{TP}R^2}\left[C^+\left(\cot\theta\,K - \frac{\partial}{\partial\theta}\right)\Psi^{JK+1}\mathcal{D}^J_{m0K+1}\right.& \\ \left. + C^-\left(\cot\theta\,K + \frac{\partial}{\partial\theta}\right)\Psi^{JK-1}\mathcal{D}^J_{m0K-1}\right].&\end{aligned} \tag{A.11}$$

By using the operators $\hat{j}_\pm$ defined in Eq. (2.13), Eq. (A.11) can be rewritten as:

$$\left[\frac{\cot\theta}{2\mu_{TP}R^2}(J_xJ_z + J_zJ_x) + \frac{\hbar}{i\mu_{TP}R^2}\left(\frac{\partial}{\partial\theta} + \frac{\cot\theta}{2}\right)J_y\right]\Psi^{JK}\mathcal{D}^J_{m0K} \tag{A.12}$$

$$= -\frac{\hbar^2}{2\mu_{TP}R^2}\left[C^+\hat{j}_-\Psi^{JK+1}\mathcal{D}^J_{m0K+1} + C^-\hat{j}_+\Psi^{JK-1}\mathcal{D}^J_{m0K-1}\right]. \tag{A.13}$$

By combining all terms diagonal in K coming from the Hamiltonian (2.35) with terms from equations (A.4)–(A.6) and rewriting $\frac{1}{\sin\theta}\frac{\partial}{\partial\theta}\sin\theta\frac{\partial}{\partial\theta} = -\hat{j}^2_\xi + \frac{K^2}{\sin^2\theta}$ one obtains:

$$\begin{aligned}&\frac{\hbar^2}{2\mu_{TP}R^2}\left[J(J+1) - K^2 + \cot^2\theta + \hat{j}^2_\xi - \frac{K^2}{\sin^2\theta}\right] \\ &+ \frac{\hbar^2}{2\mu_{12}\xi^2}\left[\csc^2\theta\,K^2 + \hat{j}^2_\xi - \frac{K^2}{\sin^2\theta}\right] - \frac{\hbar^2}{2\mu_{TP}R^2}\frac{\partial}{\partial R}R^2\frac{\partial}{\partial R} - \frac{\hbar^2}{2\mu_{12}\xi^2}\frac{\partial}{\partial\xi}\xi^2\frac{\partial}{\partial\xi} \\ &= \frac{\hbar^2}{2\mu_{TP}R^2}\left[J(J+1) - 2K^2 + \hat{j}^2_\xi\right] \\ &+ \frac{\hbar^2}{2\mu_{12}\xi^2}\hat{j}^2_\xi - \frac{\hbar^2}{2\mu_{TP}R^2}\frac{\partial}{\partial R}R^2\frac{\partial}{\partial R} - \frac{\hbar^2}{2\mu_{12}\xi^2}\frac{\partial}{\partial\xi}\xi^2\frac{\partial}{\partial\xi}.\end{aligned} \tag{A.14}$$

Finally, by multiplying (A.12) and (A.14) by $\mathcal{D}^{J*}_{MK'}$ and integrating over the Euler angles one obtains:

$$-\frac{\hbar^2}{2\mu_{TP}R^2}C^{\pm}\hat{j}_{\mp}\Psi^{JK\pm1}\delta_{K'K\pm1} \tag{A.15}$$

corresponding to Eq. (2.11) and

$$\left[\frac{\hbar^2}{2\mu_{TP}R^2}[J(J+1)-2K^2+\hat{j}_\xi^2]+\frac{\hbar^2}{2\mu_{12}\xi^2}\hat{j}_\xi^2-\frac{\hbar^2}{2\mu_{TP}}\frac{\partial^2}{\partial R^2}-\frac{\hbar^2}{2\mu_{12}}\frac{\partial^2}{\partial\xi^2}\right]\Psi^{JK}\delta_{K'K} \tag{A.16}$$

which corresponds to Eq. (2.10).

Appendix B

Numerical solution of the Schrödinger equation

There are two different approaches to the study of the quantum dynamics of a system: to solve an eigenvalue equation with a time independent Hamiltonian, or to solve the time dependent Schrödinger equation that governs the evolution of the system in time. To solve the eigenvalue equation, first the Hamiltonian of the system is represented in a basis set of size N and then the resulting matrix is diagonalised. The number of operations needed to perform the complete diagonalization of the Hamiltonian matrix scales as $\sim N^3$ while the memory required as $\sim N^2$. The number of basis functions which are needed to represent the wave function scales approximately exponentially with the dimensionality of the system. It is clear then that the main disadvantage of studying the dynamics of a system by diagonalising the Hamiltonian matrix is the fact that, for large systems, the calculation becomes not feasible in terms of computational resources. Solving the time dependent Schrödinger equation becomes a good alternative, being numerically more efficient since both the number of operations and memory requirements scale as $\sim N$ [58].

The time dependent Schrödinger equation:

$$\mathrm{i}\hbar\frac{\partial\,\Psi}{\partial\,t} = \hat{H}\Psi \tag{B.1}$$

has the formal solution

$$\Psi(t) = \mathrm{e}^{-\frac{\mathrm{i}}{\hbar}\hat{H}(t-t_0)}\Psi(t_0) = \hat{U}(t,t_0)\Psi(t_0), \tag{B.2}$$

where $\hat{U}(t,t_0)$ is the evolution operator. The procedure to find the numerical solution of Eq. (B.1) consists of two steps:

- to construct the initial wave function $\Psi(t_0)$ in a given representation
- to approximate the action of $\hat{U}(t,t_0)$ on the initial wave function

Pseudospectral methods approximate the wave function as a finite expansion over a basis of smooth functions which satisfy the appropriate boundary conditions for the specific problem [59]:

$$\Psi(x) \approx \tilde{\Psi}(x) = \sum_{j=1}^{N} a_j g_j(x) \tag{B.3}$$

Once the basis functions are chosen, the determination of the coefficients a_j can be done in different ways. One of them is the *collocation method* which is based on the requirement that the approximate solution has to match the true wave function at the grid points,:

$$\tilde{\Psi}(x_k) = \Psi(x_k) = \sum_j a_j g_j(x_k), \tag{B.4}$$

or, written in the matrix form:

$$\Psi = Ga. \tag{B.5}$$

If the basis functions g_j are orthogonal, the matrix G is unitary and Eq. (B.5) can be directly inverted leading to an expression for the expansion coefficients:

$$a_j = \sum_k g_j^*(x_k)\Psi(x_k) \tag{B.6}$$

Eq. (B.6) means that the expansion coefficients are the discrete functional transform of Ψ.

The action of an operator on the wave function is defined by the mapping of the wave function Ψ on another state vector Φ:

$$\Phi = \hat{O}\Psi. \tag{B.7}$$

On the grid, Eq. (B.7) becomes:

$$\Phi(x_i) = \sum_j^N O_{ij}\Psi(x_j), \tag{B.8}$$

which means that the mapping has to be recast in the original grid representation. Local operators in a coordinate-space grid, such as the potential operator $\hat{V}$, are diagonal and the result of their action on the wave function is simply:

$$\Phi(x_i) = V(x_i)\Psi(x_i). \tag{B.9}$$

The action of non-local operators such as the kinetic energy operator, is calculated employing the property of the basis functions g_j to be differentiable anywhere. Thus, on the grid points the derivative of the wave function is:

$$\left.\frac{\partial\,\Psi}{\partial\,x}\right|_{x_i} = \sum_n \frac{\partial}{\partial\,x} g_n(x_i) \sum_j G_{nj}^{-1}\Psi_j. \tag{B.10}$$

If the derivatives of the basis functions can be expressed in terms of the grid representation, i.e.,

$$\frac{\partial\, g_n(x)}{\partial\, x} = \sum_m d_{nm} g_m(x) \tag{B.11}$$

then, defining the derivative operator matrix as:

$$\frac{\partial\, \Psi}{\partial\, x_i} = \sum_j D_{ij} \Psi(x_j) \tag{B.12}$$

Eq. (B.10) can be expressed in matrix form as:

$$D = GdG^{-1}. \tag{B.13}$$

In this context it is useful to show the application of this formalism choosing a specific kind of basis functions. I will briefly describe two kinds of collocation methods: the Fourier method [60] and the Discrete Variable Representation DVR [61].

The basis functions $g_n(x)$ used in the Fourier method are:

$$g_k(x) = \mathrm{e}^{\frac{2\pi\,\mathrm{i}kx}{L}}, \tag{B.14}$$

where an evenly spaced grid of N points $x_j = (j-1)\Delta\, x$, $j = 1, \ldots, N$ is constructed in coordinate space with $\Delta\, x = \frac{L}{N}$ the spacing between points and $k = (-\frac{N}{2} - 1), ...0, ...\frac{N}{2})$. The wave function is then given as:

$$\Psi(x) = \sum_k a_k \mathrm{e}^{\frac{2\pi\,\mathrm{i}kq}{L}} \tag{B.15}$$

and using the orthogonality relation of the basis functions, the expansion coefficients a_k are obtained as:

$$a_k = \frac{1}{N} \sum_j \Psi(x_j) \mathrm{e}^{-\frac{2\pi\,\mathrm{i}kx_j}{L}}. \tag{B.16}$$

From Eq. (B.15) and Eq. (B.16) it is evident that the coefficients are the discrete analogues of the continuous Fourier transform, which transforms the wave function from coordinate to momentum space:

$$\Psi(x) = \frac{1}{\sqrt{2\pi}} \int_{-\inf}^{\inf} \mathrm{e}^{\mathrm{i}kx} \tilde{\Psi}(k) dk \tag{B.17}$$

$$\tilde{\Psi}(k) = \frac{1}{\sqrt{2\pi}} \int_{-\inf}^{\inf} \mathrm{e}^{-\mathrm{i}kx} \Psi(x) dx. \tag{B.18}$$

This means that the expansion coefficients a_k are interpreted as the values that the wave function takes in the momentum representation at the points p_k which form an evenly spaced grid in momentum space. This grid is connected to the coordinate-space grid by $\Delta p = \frac{2\pi}{\Delta x L}$. The use of the fast algorithms which are available now to compute the discrete Fourier transformations (Fast Fourier Transform - FFT) makes this kind of pseudospectral method very numerically efficient. Indeed, the computational effort for the generation of the a_k coefficients scales as $\mathcal{O}(N \log N)$ as this is the general scaling property of the FFT method.

Another important advantage of using the Fourier method is that the basis functions g_k are eigenfunctions of the derivative matrix which means that the matrix elements d_{nm} are immediately known: $d_{nm} = \frac{2\pi \mathrm{i}}{L}\delta_{nm}$. The matrix G is unitary ($G^{-1} = G^{\dagger}$) thus Eq. (B.13) becomes analogous to the expression for the Fourier derivative:

$$\frac{\partial \Psi}{\partial x} = \frac{1}{2\pi} \int_{-\inf}^{\inf} \mathrm{i}k \mathrm{e}^{\mathrm{i}kx} \tilde{\Psi}(k) \mathrm{d}k \tag{B.19}$$

This analogy is understood in terms of the similarity between the matrix G and the transformation matrix between coordinate and momentum space $\langle px \rangle$. In momentum space, the derivative operator is diagonal and its action on the wave function is simply a multiplication. Thus, an efficient strategy to compute the action of the kinetic energy operator on the wave function consists in transforming the wave function to momentum space and multiplying it by the kinetic energy operator

$$\hat{T}\tilde{\Psi}(k) = \frac{\hbar^2 k^2}{2m} a_k \tag{B.20}$$

and performing Fourier transform of the result back to the coordinate space.

Another of the collocation methods which is widely used is the DVR. This representation employs basis functions which are approximately localised around the grid points. There are different ways to construct such a basis set: to diagonalize a given matrix representation of the position operator $\langle \phi_n | \hat{x} | \phi_m \rangle$ and then to choose, among all such bases which can be obtained from a unitary transformation of the $|\phi_n\rangle$, the one which minimizes the location criterion [58]:

$$\sum_n (\langle x_n | \hat{x}^2 | x_n \rangle - \langle x_n | \hat{x} | x_n \rangle^2) \rightarrow \min \tag{B.21}$$

Typical choices for the $|\phi_n\rangle$ are the harmonic oscillator eigenfunctions (Hermite polynomials) for the radial part and Legendre polynomials for the angular part. Once the basis

functions are constructed the action of an operator on the wave function is calculated. Operators which are functions of the coordinates act on the wave function by multiplication. For operators involving derivatives, such as the kinetic energy operator, a prescription can be obtained starting from Eq. (B.10)-(B.13). In Appendix A of [62], the derivation of the expression for the kinetic energy operator within the DVR scheme is derived.

The key point of this discussion is to show that in order to compute the action of the Hamiltonian on the wave function one can proceed by different ways accordingly for different representations of the wave function on a numerical grid. In my work, I used the Fourier method over the DVR approach to take advantage of the high efficiency of the Fourier method due to the scaling property of the FFT algorithm.

As an example I will describe the method to compute the action of one specific operator – the time evolution operator:

$$\hat{U}(t, t_0) = \mathrm{e}^{\frac{-\mathrm{i}}{\hbar}\hat{H}(t-t_0)}, \tag{B.22}$$

with Hamiltonian $\hat{H}$. I focus on this operator because I am interested in solving the time-dependent Schrödinger equation. Several methods are available, but I will focus on the one I implemented in this work – the *Chebychev propagator* method.

In the Chebychev propagator method the time evolution operator is approximated by a finite sum over complex Chebychev polynomials T_n. The polynomials are defined on the interval $[-\mathrm{i}, \mathrm{i}]$ and their argument has to be first rescaled to lie within the domain of the polynomials:

$$z' = \frac{\overline{E} - z}{\Delta E}, \tag{B.23}$$

where $\overline{E} = (\lambda_{\max} + \lambda_{\min})/2$ and $\Delta E = (\lambda_{\max} - \lambda_{\min})/2$ with $\lambda_{\min,\max}$ being the smallest and largest values the function can acquire on the grid. The expansion of the function $f(z)$ to be approximated is:

$$f(z) = \sum_{n}^{N} b_n T_n(z'), \tag{B.24}$$

where the expansion coefficients b_n are defined as:

$$b_n = \frac{2 - \delta_{n0}}{\pi} \int_{-1}^{1} \frac{f(z')T_n(z')}{\sqrt{1 - z'^2}} \tag{B.25}$$

The Chebychev polynomials are constructed by recursive relation:

$$T_{n+1} + T_{n-1} - 2T_n = 0 \tag{B.26}$$

with initial values:

$$T_0 = 1 \tag{B.27}$$

$$T_1 = z' \tag{B.28}$$

In the case of evolution operator (B.22), the function to be approximated is the action of $\hat{U}(t, t_0)$ on the wave function, i.e. $\phi = f(\hat{H})\Psi = \mathrm{e}^{-\frac{\mathrm{i}}{\hbar}\hat{H}(t-t_0)}\Psi$. The spectral range of the Hamiltonian has to be adapted to fit within the domain of Chebychev polynomials and a linear transformation:

$$\hat{H}_{\mathrm{norm}} = \frac{\overline{E}\hat{I} - \hat{H}}{\Delta E} \tag{B.29}$$

is performed with $\lambda_{\mathrm{min,max}}$ being the smallest and largest eigenvalues supported by the numerical grid. The function of $\hat{H}$ is in this case the evolution operator (B.22) and the expansion coefficients are:

$$b_n = (2 - \delta_{n0})\mathrm{i}^n J_n\left(\frac{\Delta E(t - t_0)}{\hbar}\right)\mathrm{e}^{-\frac{\mathrm{i}}{\hbar}\overline{E}(t-t_0)}, \tag{B.30}$$

where J_n are Bessel functions. The number of terms N needed to reach convergence of the expansion (B.24) is determined by the volume of time–energy phase space which is the argument of the Bessel function. When the order n is larger than the argument of J_n the Bessel functions decrease exponentially. This means that for $n > \Delta H(t - t_0)/\hbar$ the expansion (B.24) converges exponentially. The exponential term appearing in Eq. (B.30) compensates for the shift in the energy scale due to the adjustment of the domain of $\hat{H}$ with respect to the domain of the Chebychev polynomials.

Appendix C

Coriolis couplings

In section 2.2 I described the reference frame used to address the problem in three dimensions. The most straightforward way would have been to work in the three-dimensional Cartesian-coordinate space spanned by a pair of relative Jacobi vectors. This would have lead to a simple representation of the Hamiltonian operator but the calculations would have been numerically inefficient due to the large dimensionality (six degrees of freedom). It is computationally more efficient to use a different coordinate representation, although the derivation of the Hamiltonian becomes more complicated. A frame of reference fixed to the system was chosen with a specific choice of the embedding that was already described in section 2.2 and the expression for the Hamiltonian operator with respect to this reference frame was presented in equations (2.10), (2.11). For a given value of total angular momentum of the system J the wave function is given as a sum over its components K (K is the z-projection of the total angular momentum) of direct products between a function of the internal coordinates R, ξ and θ and an element of the Wigner D-matrix which depends on the Euler angles. The central point is to calculate the action of the different operators contained in the Hamiltonian on the wave function. In appendix B it was explained how to compute the action of operators which depends on the spatial coordinates and on their derivatives. But one has to evaluate the action of $\hat{j}_\xi^2$ and $\hat{j}_\pm$ as well.

Essentially, a DVR representation for $\hat{j}_\xi^2$ and $\hat{j}_\pm$ is constructed employing the associated Legendre polynomials $\tilde{P}_J^K(\cos(\theta_\alpha))$ as basis functions. A grid of θ_α points is built where the points are obtained by the diagonalization of $\cos(\hat{\theta})$ in the basis $\{\tilde{P}_J^{K=0}\}_{J=0}^{J_{\mathrm{MAX}}}$ together with the weights w_α. The transformation which relates the basis functions to the grid points is given by:

$$U_{J\alpha}^K = \sqrt{w}_\alpha \tilde{P}_J^K(\cos(\theta_\alpha)). \tag{C.1}$$

I will now only provide the final expressions for the action of the operators on the wave function in the DVR representation, more details about the DVR representations of these

operators can be found in [63]:

$$\hat{j}_\xi^2\phi(\theta_\alpha, K) = \sum_\beta^N \hat{j}_\xi^2(\alpha, \beta, K)\phi(\theta_\beta, K) \tag{C.2}$$

$$\hat{j}_\pm\phi(\theta_\alpha, K \pm 1) = \sum_\beta^N \hat{j}_\pm(\alpha, \beta, K)\phi(\theta_\beta, K) \tag{C.3}$$

where $\hat{j}_\xi^2(\alpha, \beta, K)$ and $\hat{j}_\pm(\alpha, \beta, K)$ are the DVR representations for the operators according to equations (31), (32) and (33) in Ref. [63].

In the following I will discuss in detail some numerical issues and related solutions which arise when evaluating the effect of the Coriolis couplings. Coriolis couplings correspond to the parts of the total Hamiltonian (2.11) which couple states with different values of K, i.e. $\Psi^{JK} \leftrightarrow \Psi^{JK\pm,1}$. The operators responsible for the coupling are:

$$\hat{j}_\pm = \mp\frac{\partial}{\partial\theta} + K\cot\theta \tag{C.4}$$

and represent lowering and raising operators associated with the projectile angular momentum in the BF frame. It was noticed in Ref. [48] that numerical issues caused by non-Hermicity of the operator (C.4) arise. The issue is due to the fact that the operators $\hat{j}_\pm$ are not Hermitian conjugate since the Jacobian of the coordinate transformation from Cartesian to the specific body-fixed frame used in section 2.2 is not constant. For the operators (C.4) one obtains:

$$\left(\frac{\partial}{\partial\theta}\right)^\dagger = -\frac{\partial}{\partial\theta} - \cot\theta, \tag{C.5}$$

which means that

$$\hat{j}_+^\dagger \neq \hat{j}_-. \tag{C.6}$$

A method to evaluate analytically the matrix elements of the operator of Eq. (C.4) that also solves the issue with non-Hermicity was presented in Ref. [48]. The two parts the operator (C.4) are considered separately and, together with operator $\csc\theta$, represented in a basis of real orthogonal polynomials $P_j(z)$ with $z = \cos\theta$. Working directly in the coordinate representation of the polynomials, i.e., $z = z(\theta) = \cos\theta$, the three operators become:

$$\begin{aligned} -\frac{\partial}{\partial\theta} &\to \sqrt{1-z^2}\frac{\partial}{\partial z}, \\ \cot\theta &\to \frac{z}{\sqrt{1-z^2}}, \\ \csc\theta &\to \frac{1}{\sqrt{1-z^2}}. \end{aligned} \tag{C.7}$$

According to Ref. [48], if the integral:

$$N_k = \int \sqrt{w(z)}\hat{A}z^k\sqrt{w(z)}\mathrm{d}z \tag{C.8}$$

can be evaluated analytically for any value of k for each operator $\hat{A}$ from (C.7), then the matrix elements $A_{jj'} = \langle\, j'|\hat{A}|j\rangle$ can be obtained using the following recursive relation:

$$P_j(z) = a_j z P_{j-1}(z) - b_j P_{j-2}(z). \tag{C.9}$$

In practice one proceeds in the following way:

- evaluating the matrix elements $A_{0j} \propto \int \sqrt{w(z)}\hat{A}P_j(z)\mathrm{d}z$ which are often available from tables
- evaluating the remaining matrix elements $A_{jj'} = \int\, P_{j'}(z)\hat{A}P_j(z)dz$ replacing $P_j(z)$ by expression (C.9)

By applying this strategy for each of the operators in (C.7) the final expression for the matrix elements of the part of the Hamiltonian containing the Coriolis coupling (Eq. (2.11)) is:

$$\langle\, J(K\pm 1)|\hat{\mathcal{H}}^J_{KK\pm 1}|JK\rangle = \frac{\hbar^2\sqrt{J(J+1)-K(K\pm 1)}}{2\mu_{TP}R^2}\left[C_{j'j}(K\pm 1) + KC_{jj'}\right], \tag{C.10}$$

where $C_{j'j} = \langle\, j'|\sqrt{1-z^2}\frac{\partial}{\partial z}|j\rangle$ are the matrix elements of the operator $-\frac{\partial}{\partial\theta}$ in the polynomial basis representation. The matrix defined by (C.10) is Hermitian as can be seen from replacing $(K \pm 1)$ by K and j' by j.

Appendix D

Initial wave function of the composite projectile

At the initial time the projectile is considered to be so far away from the target that the interaction with it is so weak that it can be neglected. Under this assumption the Hamiltonian of the system becomes separable and the initial wave function can be written as a direct product of the wave function that describes the ground state of the projectile and a Gaussian wave packet which describes the projectile center of mass motion. The ground state of the projectile is determined by solving the eigenvalue equation:

$$\left[\frac{-\hbar^2}{2\mu_{12}}\nabla^2_{\vec{\xi}} + U_{12}(\xi)\right]\chi_n(\vec{\xi}\,) = E_n\chi_n(\vec{\xi}\,), \tag{D.1}$$

where $\xi = \|\vec{\xi}\|$ and $U_{12}(\xi)$ is the part of the total Hamiltonian (2.1) which depends only on the coordinate $\vec{\xi}$, describing the relative motion between the projectile fragments; and μ_{12} is the reduced mass of the projectile constituents 1 and 2. In my case the potential $U_{12}(\xi)$ has simple Woods–Saxon form, is spherically symmetric, and the standard procedure of separating the radial and angular degrees of freedom in spherical coordinates can be applied. The ground state solution, where the angular quantum number $l = 0$, has a trivial (constant) angular part and only the radial part of the wave function $\tilde{\chi}(\xi)$ needs to be found:

$$-\frac{\hbar^2}{2\mu_{12}}y''(\xi) + U(\xi)y(\xi) = E_0 y(\xi), \tag{D.2}$$

where $y(\xi) = \xi\tilde{\chi}(\xi)$. Such equation can be easily solved by the *Numerov method* [64] suitable for second order linear differential equations of the form:

$$y''(\xi) + Q(\xi)y(\xi) = 0. \tag{D.3}$$

In my case $Q(\xi) = \frac{2\mu_{12}}{\hbar^2}(E_0 - U_{12}(\xi))$. First, the function y is discretized and represented in terms of its values at the grid points $\{\xi_i\}_1^N$, $y(\xi) \to y(\xi_i) \equiv y_i$. In this notation, Eq. (D.3) becomes:

$$y_i'' + Q_i y_i = 0. \tag{D.4}$$

The Taylor expansion of the solution y at the point $(\xi + h)$ around ξ gives:

$$y(\xi + h) = y(\xi) + h\frac{\mathrm{d}}{\mathrm{d}\xi}y + \frac{h^2}{2}\frac{\mathrm{d}^2}{\mathrm{d}\xi^2}y + \frac{h^3}{6}\frac{\mathrm{d}^3}{\mathrm{d}x^3}y + \frac{h^4}{24}\frac{\mathrm{d}^4}{\mathrm{d}x^4}y + ... \tag{D.5}$$

Making the equivalent expansion for $y(\xi - h)$, denoting $y(\xi \pm h) = y_{i\pm 1}$, and substituting it to Eq. (D.5) the following expression for y_{i+1} is obtained:

$$y_{i+1} = 2y_i - y_{i=1} + h^2\frac{\mathrm{d}^2}{\mathrm{d}x^2}y_i + \frac{h^4}{12}\frac{\mathrm{d}^4}{\mathrm{d}x^4}y_i + \mathcal{O}(h^6). \tag{D.6}$$

Defining now

$$\frac{\mathrm{d}^2}{\mathrm{d}x^2}y_i = F_i \tag{D.7}$$

Eq. (D.6) becomes:

$$y_{i+1} - 2y_i = y_{i-1} + h^2F_i + \frac{h^4}{12}\frac{\mathrm{d}^2}{dx^2}F_i + \mathcal{O}(h^6). \tag{D.8}$$

From this equation, the three point central difference formula for the second derivative is obtained:

$$y'' = \frac{y_{i+1} + y_{i-1} - 2y_i}{h^2}. \tag{D.9}$$

Taking the second derivative of Eq. (D.4), substituting it for $\frac{\mathrm{d}^2}{\mathrm{d}x^2}F_i$:

$$\frac{\mathrm{d}^2}{\mathrm{d}x^2}F_i = -\frac{\mathrm{d}^2}{\mathrm{d}x^2}(Q_iy_i), \tag{D.10}$$

and using Eq. (D.9) for the second derivative of $F_i = -Q_iy_i$, one obtains:

$$\frac{\mathrm{d}^2}{\mathrm{d}x^2}F_i = -\frac{1}{h^2}\left(Q_{i+1}y_{i+1} + Q_{i-1}y_{i-1} - 2Q_iy_i\right) + \mathcal{O}(h^2). \tag{D.11}$$

Finally, by combining Eq. (D.11) and Eq. (D.8) one obtains the following three-term recursive relation:

$$\left(1 + \frac{h^2}{12}Q_{i+1}\right)y_{i+1} = 2\left(1 - \frac{5h^2}{12}Q_i\right)y_i - \left(1 + \frac{h^2}{12}Q_{i-1}\right)y_{i-1} + \mathcal{O}(h^6). \tag{D.12}$$

Having two consecutive values of y_i, it is possible to generate the entire solution.

The radial Schrödinger equation (D.2) is; however, an eigenvalue equation, i.e. both the solution $y(\xi)$ and the eigenvalue E_0 are to be found. Bound-state solution of Eq. (D.2) behaves like ξ^{l+1} ($l = 0$ for the ground state) near the origin $\xi = 0$ which serves as the initial condition for the recursive relation (D.12). By integrating from the origin the solution of (D.2) can be found for every parameter E_0, resulting in either exponentially diverging or regular solutions for large ξ [65]. The condition of square-integrability of the wave function is used to find the eigenvalues by simply minimizing the norm of the wavefunction [65].